

Modelling mass distribution in elliptical galaxies: mass profiles and their correlation with velocity dispersion profiles

Kyu-Hyun Chae^{1*}, Mariangela Bernardi² and Andrey V. Kravtsov^{3,4}

¹*Sejong University, Department of Astronomy and Space Science, 98 Gunja-dong, Gwangjin-Gu, Seoul 143-747, Republic of Korea*

²*Department of Physics and Astronomy, University of Pennsylvania, 209 South 33rd Street, Philadelphia, PA 19104, USA*

³*Kavli Institute for Cosmological Physics, 5640 South Ellis Avenue, The University of Chicago, Chicago, IL 60637, USA*

⁴*Department of Astronomy and Astrophysics, 5640 South Ellis Avenue, The University of Chicago, Chicago, IL 60637, USA*

**chae@sejong.ac.kr*

Accepted Received; in original form

ABSTRACT

We assemble a statistical set of global mass models for $\sim 2,000$ nearly spherical Sloan Digital Sky Survey (SDSS) galaxies at a mean redshift of $\langle z \rangle = 0.12$ based on their aperture velocity dispersions and newly derived luminosity profiles in conjunction with published velocity dispersion profiles and empirical properties and relations of galaxy and halo parameters. When two-component (i.e. stellar plus dark) mass models are fitted to the SDSS aperture velocity dispersions, the predicted velocity dispersion profile (VP) slopes within the effective (i.e. projected half-light) radius R_{eff} match well the distribution in observed elliptical galaxies. From a number of input variations the models exhibit for the radial range $0.1R_{\text{eff}} < r < R_{\text{eff}}$ a tight correlation $\langle \gamma_e \rangle = (1.865 \pm 0.008) + (-4.93 \pm 0.15)\langle \eta \rangle$ where $\langle \gamma_e \rangle$ is the mean slope absolute value of the total mass density and $\langle \eta \rangle$ is the mean slope of the velocity dispersion profile, which leads to a super-isothermal $\langle \gamma_e \rangle = 2.15 \pm 0.04$ for $\langle \eta \rangle = -0.058 \pm 0.008$ in observed elliptical galaxies. Furthermore, the successful two-component models appear to imply a typical slope curvature pattern in the total mass profile because for the observed steep luminosity (stellar mass) profile and the weak lensing inferred halo profile at large radii a total mass profile with monotonically varying slope would require too high DM density in the optical region giving rise to too large aperture velocity dispersion and too shallow VP.

Key words: galaxies: kinematics and dynamics – galaxies: structure – galaxies: haloes – galaxies: formation

1 INTRODUCTION

Observed galaxies exhibit substantial diversity in their morphological appearances and structure. Early-type, namely elliptical and lenticular, galaxies (ETGs) are more massive on average among galaxy types and are thought to originate from mergers of late-type galaxies and smaller ETGs under the paradigm of hierarchical galaxy formation and evolution (e.g., Press & Schechter 1974; White & Rees 1978). The empirical properties of ETGs hold important clues to the physical processes shaping properties of the most massive galaxies. ETGs also play a crucial role in modern cosmology including dark energy phenomenology. Owing to their large masses and high central densities ETGs dominate observed population of strong lenses and are also important for weak lensing which provide both geometric (through cosmologi-

cal distances) and dynamical (through growth of structures) probe of dark energy (Frieman, Turner & Huterer 2008). Massive ETGs, or similarly luminous red galaxies by colour selection, are also excellent targets of the baryonic acoustic oscillation studies that provide an independent cosmological probe of the distance scale in the universe (e.g., Eisenstein et al. 2005; Percival et al. 2007; Sánchez et al. 2012).

For both astrophysical and cosmological studies involving ETGs, their density structure, in particular the radial profile, is of great importance for several reasons. First of all, as the radial mass profile encodes the combined distribution of luminous and dark matter, it is a key quantity to constrain galaxy formation and evolution models. An important question is whether there is a simple natural attractor of radial density profile such as the Navarro-

Frenk-White (NFW) profile (e.g., Navarro, Frenk & White 1997; Loeb & Peebles 2003) or the isothermal profile (e.g., Lynden-Bell 1967; Gerhard et al. 2001; Chae 2011). Secondly, because there is no empirical method to directly measure dark matter (DM) distribution in a galaxy, accurate determination of the total mass profile is the crucial first step toward the inference of DM distribution (e.g., Newman et al. 2013). Finally, the radial mass profile is a crucial factor in gravitational lensing (both strong and weak). Strong lensing image flux ratios depend largely on the radial density slope at the Einstein radius. Weak lensing by individual haloes and large-scale structures depend on the global radial profile of galaxies and clusters.

The radial total mass profile of a galaxy can be constrained using dynamic probes such as stellar or gas dynamics, or gravitational lensing. For nearby ETGs stellar dynamics has been the most fruitful probe because detailed stellar kinematic data as well as photometric data are available. Detailed dynamical models based on the observed luminosity distributions and stellar velocity moments have been constructed for tens to hundreds ETGs (e.g., Gerhard et al. 2001; Thomas et al. 2007; Cappellari et al. 2013a). For nearby X-ray bright massive ellipticals, hydrostatic equilibrium equation has been used to infer mass profiles (e.g., Das et al. 2010). The inferred mass profiles from these studies in general exhibit significant variation of the logarithmic slope with radius, although the density profiles are close to isothermal around the half-light radius of stellar distribution. Nevertheless, the sample sizes of dynamical and lensing studies of mass distribution in the ETGs have been fairly small to allow systematic study of profile variation in a wide radial range.

Strong lensing studies have been used to constrain the total mass profile of distant galaxies at various redshifts (e.g., Rusin, Kochanek & Keeton 2003; Barnabè et al. 2011; Ruff et al. 2011; Bolton et al. 2012). Strong lensing effectively constrains the density slope (absolute value) γ ($\equiv -d \ln \rho / d \ln r$) or, more precisely, the slope of the projected 2-dimensional density γ_{2D} , at the Einstein radius R_{Ein} , which increases with redshift at fixed R_{eff} : e.g., $R_{\text{Ein}} \sim 0.5 R_{\text{eff}}$ at $z = 0.1$ but $R_{\text{Ein}} \sim R_{\text{eff}}$ at $z = 0.6$ (Bolton et al. 2012). For systematic analyses of samples of tens of strong lens systems constant- γ models have usually been adopted and the constrained values of γ have mean slopes close to the isothermal value $|\langle \gamma \rangle - 2| < 0.1$ for $0.2 \lesssim z \lesssim 1$ (e.g., Rusin, Kochanek & Keeton 2003; Barnabè et al. 2011). However, recently it was noticed that the value of γ appeared to evolve significantly with z based on combined samples that contain both low $z \sim 0.1$ lenses and intermediate $z \sim 0.6$ lenses (Bolton et al. 2012; Ruff et al. 2011). Assuming γ was independent of radius in the optical region, the apparent redshift evolution of γ was interpreted in terms of galaxy evolution. Notably, the apparent evolution implies $\langle \gamma \rangle \approx 2.3$ at $z = 0$ (Bolton et al. 2012). Finally, stellar dynamics, strong and weak lensing were combined to infer the total mass profile for a large radial range for several individual systems (Newman et al. 2013) or stacked data (Gavazzi et al. 2007). The former work focused on galaxy clusters, while the latter study used only the de Vaucouleurs stellar mass profile and the NFW DM profile without taking into account halo contraction effects by

baryonic physics (e.g., Blumenthal et al. 1986; Gnedin et al. 2004; Sellwood & McGaugh 2005; Gnedin et al. 2011).

From recent dynamical analyses of ETGs it is not clear whether the isothermal model is a good approximation to the average profile for some radial range or whether the average profile is systematically varying with redshift or some other parameter. Here we investigate galaxy mass profile through Jeans dynamical analyses based on Sloan Digital Sky Survey (SDSS; York et al. 2000) galactic luminosity distributions and aperture velocity dispersions in conjunction with published velocity dispersion profiles and empirical properties and relations for ETGs and their haloes. SDSS photometric data and aperture velocity dispersions have been useful in addressing several issues including estimating dynamical masses and dark matter contents within R_{eff} (e.g., Padmanabhan et al. 2004; Tortora et al. 2012), testing halo contraction/expansion models and stellar initial mass functions (IMFs) (Dutton et al. 2011, 2013; Dutton & Treu 2013). These studies confirm that non-negligible amount of dark matter is generally required within R_{eff} and suggest that the DM fraction within R_{eff} is correlated with properties such as surface brightness and R_{eff} and galaxies require non-universal IMFs or/and non-universal dark halo response to galaxy formation. Our present study of SDSS ETGs has the following aspects. First, we select nearly spherical and disk-less galaxies for our analyses by the spherical Jeans equation so that any possible systematic errors due to non-spherical shapes, which were ignored in all previous analyses, can be minimized. Second, the main focus of our work is galaxy total mass profile and for that purpose we use an empirical distribution of velocity dispersion profiles (VPs) within R_{eff} . Third, we use newly measured luminosity profile parameters, Sersic index n and effective radius R_{eff} . Fourth, we take into account recently published systematic IMF variation in early-type galaxies. Finally, our analyses are based on real data and auxiliary empirical inputs excluding simulation or theoretical inputs. Our present work has a different focus and is an improvement with updated and more reliable inputs compared with Chae et al. (2012) which considered VPs but focused on DM profiles with inputs from N-body simulations.

For our Jeans analyses we assume parametric functional forms for the total mass profile. When a model is fitted to the aperture velocity dispersion, it predicts a velocity dispersion profile. We then compare the predicted distribution of VPs with the empirical distribution to test the model. Our successful models are two-component models in which stellar mass distribution is assumed to follow the photometrically derived luminosity profile and the coupled DM distribution is assumed to follow the gNFW or Einasto model, which are motivated from cosmological hydrodynamic simulations of galaxy formation, with the constraint that they match weak lensing observations at large radii. Our model set is at least an order of magnitude larger than any previous set of empirical (as opposed to simulation or semi-empirical) models for ETGs. In addition, it covers a large radial range extending from $\sim 0.1 R_{\text{eff}}$ to the halo virial radius.

The outline of this paper is as follows. In section 2 we describe our data and other empirical results from the literature that are needed for our analyses. In section 3 we describe mass model parametrisation and method of Jeans dynamical analyses. In section 4 we describe statistical re-

sults for mass profiles based on standard empirical inputs and then in section 5 we consider systematic variations of the statistical results. In section 6 we compare our results with recent results based on SDSS photometric data and aperture velocity dispersions. In sections 7 & 8 we discuss implications of our results for galaxy formation and strong lensing. We conclude in section 9.

2 GALAXY DATA AND EMPIRICAL RELATIONS

We carefully define a sample of nearly spherical (projected minor-to-major axis ratio $b/a > 0.85$) and diskless (disk mass is within the measurement error of total mass) galaxies with mean redshift $\langle z \rangle \approx 0.12$ selected from the SDSS (Bernardi et al. 2010, 2012; Meert, Vikram & Bernardi 2012). This selection excludes all lenticular and later-type galaxies, while retaining galaxies spanning two orders of magnitude in stellar mass ($10 \lesssim \log_{10}(M_*/M_\odot) \lesssim 12$), and was chosen to minimize biases in analyses based on the spherical Jeans equation (see section 3). Therefore, our resulting mass profiles will apply strictly to nearly spherical galaxies only. However, we will also consider modelling a general sample of ETGs to estimate any systematic difference in mass profile between our nearly spherical sample and a general sample.

Because each galaxy in our sample has a nearly spherical component only, its luminosity profile can generally be well described by a single-component Sérsic (1968) profile, except possibly for the sub-kiloparsec central region (see below). Each galaxy has the surface brightness Sérsic-fit effective radius R_{eff} , the Sérsic index n , the luminosity-weighted line-of-sight velocity dispersion (LOSVD) within the SDSS aperture of radius 1.5 arcsec σ_{ap} and the total stellar mass M_*^{Ch} converted from the measured luminosity using the Chabrier (Chabrier 2003) stellar initial mass function (IMF) or equivalently mass-to-light (M/L) ratio. Recent observational studies have found that IMFs of ETGs are not universal but show galaxy-to-galaxy scatter and systematic trends with some parameters such as stellar velocity dispersion (VD) σ . To encompass the current likely range we use three independently inferred σ -dependent IMFs (e.g., Cappellari et al. 2013b; Conroy & van Dokkum 2012; Tortora, Romanowsky & Napolitano 2013; see section 2.3).

It is well-known that the central sub-kiloparsec region of ETG light profile exhibits large variation giving rise to either the central missing light due to the shallower core or the central extra light due to the steeper power-law profile compared with the main body profile extrapolation (e.g., Faber et al. 1997; Hyde et al. 2008; Kormendy et al. 2009; Glass et al. 2011). This central extra or missing light can have non-negligible effects for small R_{eff} galaxies. However, SDSS photometric data do not have enough resolution for the central regions of our $\langle z \rangle \approx 0.12$ galaxies. To allow for the observed deviations in the central regions from the overall Sérsic profiles for ETGs we use the central profile properties, i.e. the break radius and the slope at a fiducial central radius as a function of stellar mass, extracted from published data including the *Hubble Space Telescope* data (see section 2.8).

Each galaxy is further assigned its halo mass M_{200}

within the virial radius r_{200} , which is defined to be the radius of the sphere within which the mean density is 200 times the cosmic mean matter density (equation 6 of Mandelbaum, Seljak & Hirata 2008),

$$r_{200} = \frac{251.6}{(1+z)} \left(\frac{M_{200}}{10^{12} h^{-1} M_\odot} \right)^{1/3} h^{-1} \text{ kpc} \quad (1)$$

assuming a flat Λ -dominated Universe with $\Omega_{\text{m}0} = 0.27$ and $h = H_0/100 \text{ km s}^{-1} = 0.7$ (Komatsu et al. 2011). For this we use the empirical M_* - M_{200} relations from SDSS satellite kinematics (More et al. 2011) and weak lensing (Schulz, Mandelbaum & Padmanabhan 2010; Mandelbaum et al. 2006), as well as the abundance matching relation (Chae et al. 2012) to encompass the current likely range (see section 2.4).

The halo assigned to each galaxy is then assigned a mass profile at large radii ($r > 0.2r_{200}$) using the weak lensing observations of the SDSS galaxies, which not only show that the outer halo profile can be well described by the NFW profile but also give the mean halo mass (M_{200})-NFW concentration (c_{NFW}) relation derived from stacked profiles (Mandelbaum, Seljak & Hirata 2008). We use an intrinsic scatter of 0.1 dex and allow $\pm 30\%$ of systematic errors.

To constrain the mass profile in the optical region of each nearly spherical galaxy we need not only the aperture VD σ_{ap} but also the VD profile. We do not have a measured VD profile for each galaxy in our sample. However, we can use an empirical statistical distribution of VD profiles from the literature (Cappellari et al. 2006; Mehlert et al. 2000) as described in section 2.6.

In the following subsections we describe in detail our data and all empirical results from the literature that are needed for our analyses.

2.1 Luminosity (stellar mass) profiles

To describe the observed light distribution of an ETG we use the Sérsic model or a two-component ('SerExp') model that contains a Sérsic bulge and an exponential disk. From the light distribution we derive the volume distribution of stellar mass using empirically derived stellar IMFs (see below section 2.3).

The Sérsic surface brightness distribution on the sky given by

$$I(X) \propto \exp\left(-b_n X^{1/n}\right), \quad (2)$$

with $X = R/R_{\text{eff}}$ (R being the two dimensional radius) and $b_n = 2n - 1/3 + 0.009876/n$ (for $0.5 < n < 10$) (Prugniel & Simien 1997) allows a more accurate description of a dispersion-supported system than the traditional de Vaucouleurs model which is the special case of $n = 4$.

More recently it has been recognized that most ETGs are better described by a compound model composed of two distinct components, namely a bulge and a disk, although the bulge is dominating (Bernardi et al. 2012; Meert, Vikram & Bernardi 2012). When a two-component system with the non-negligible disk is fitted by a single Sérsic model, the resulting parameters, in particular galaxy size R_{eff} , can be biased compared with the actual bulge parameters (Bernardi et al. 2012; Meert, Vikram & Bernardi 2012). The bias in R_{eff} is less than 0.05 dex for stellar mass

$\lesssim 10^{11.5} M_{\odot}$ but can be as large as 0.08 dex near the high mass tail (Bernardi et al. 2012).

For our Jeans analyses we select nearly spherical and disk-less systems that are well-described by the single-component Sérsic profiles (see, however, section 2.8 for the profiles of the central sub-kpc regions). However, we also consider modelling general ETGs to estimate possible systematic difference of our results from those for general ETGs. In this case we use the single Sérsic fit to the total light distribution. When we use the single Sérsic fit for a galaxy having a non-negligible disk, we are using a biased R_{eff} as mentioned above.

2.2 SDSS samples of ETGs

We select a sample of 28,259 ETGs from the SDSS main galaxy sample satisfying light concentration $C_r > 2.6$ and $n_{\text{bulge}} > 2.5$ where C_r is the ratio of the radius containing 90 percent of the Petrosian luminosity in the r -band to that containing 50 percent (Bernardi et al. 2010) and n_{bulge} is the bulge Sérsic index in the SerExp fit of the total light distribution. A subsample of 20,210 ETGs satisfies $C_r > 2.86$. Each galaxy in the sample has aperture velocity dispersion σ_{ap} and ellipticity ε ($\equiv 1 - b/a$ with b/a being the projected minor-to-major axis ratio) as well as fitted parameters of both the Sérsic and the SerExp models along with corresponding stellar masses based on the Chabrier IMF. The Sérsic-fit parameters are M_{\star}^{Ch} (total stellar mass based on the Chabrier IMF), R_{eff} (effective radius) and n (Sérsic-fit index). The SerExp-fit parameters are $M_{\text{bulge},\star}^{\text{Ch}}$ (bulge stellar mass based on the Chabrier IMF), $R_{\text{bulge,eff}}$ (bulge effective radius), n_{bulge} (bulge Sérsic-fit index) as well as M_{\star}^{Ch} and R_{eff} for the total (bulge plus exponential) profile.

Based on the observed light distributions and the model fitted parameters we select a $C_r > 2.86$ subsample of 2,054 nearly spherical and disk-less ellipticals using the criteria $\varepsilon < 0.15$ (single Sérsic-fit ellipticity) and $\log_{10}(R_{\text{eff}}/R_{\text{bulge,eff}}) < 0.19$ (the sum of the estimated measurement errors for R_{eff} in the single Sérsic fit and $R_{\text{bulge,eff}}$ in the SerExp fit). Galaxies in this sample have the following properties $\log_{10}(M_{\star}^{\text{Ch}}/M_{\text{bulge},\star}^{\text{Ch}}) = 0.064 \pm 0.049$, $\log_{10}(R_{\text{eff}}/R_{\text{bulge,eff}}) = 0.062 \pm 0.085$ and $\varepsilon = 0.089 \pm 0.039$. The distribution of redshifts and the physical aperture to effective radius ratios $R_{\text{ap}}/R_{\text{eff}}$ can be found in Fig. 1. The redshift distribution has a mean of $\langle z \rangle \approx 0.12$ with a root-mean-square (RMS) dispersion of $s_z \approx 0.05$ while the $R_{\text{ap}}/R_{\text{eff}}$ distribution has $\langle R_{\text{ap}}/R_{\text{eff}} \rangle \approx 0.53$ and $s_{R_{\text{ap}}/R_{\text{eff}}} \approx 0.23$. Another important feature of this sample is that galaxies have higher Sérsic indices compared with other ETG samples in the literature: we have $\langle n \rangle \approx 5.1$ (with $s_n \approx 1.1$) compared with $\langle n \rangle \approx 3.6$ for 260 ATLAS^{3D} galaxies (Krajnović et al. 2013). (See further section 6.) This sample will be our standard (fiducial) choice because our analysis is based on the spherical Jeans equation. Other samples will be used to estimate systematic errors of galaxy sampling. In particular, we also consider a $C_r > 2.6$ subsample of 2,607 nearly spherical and disk-less ellipticals to see the effects of varying the ETG selection criterion. The $C_r > 2.6$ subsample has a somewhat lower Sérsic mean, $\langle n \rangle \approx 4.7$.

The above measured parameters are uncertain to varying degrees. Our formal estimates of the measurement er-

rors are: $s_{\log \sigma_{\text{ap}}} \approx 0.04$; $s_{\log M_{\star}^{\text{Ch}}} \approx 0.1$, $s_{\log M_{\text{bulge},\star}^{\text{Ch}}} \approx 0.2$; $s_{\log R_{\text{eff}}} \approx 0.04$ at $\log_{10}(M_{\star}^{\text{Ch}}/M_{\odot}) = 10.5$ varying to ≈ 0.07 at $\log_{10}(M_{\star}^{\text{Ch}}/M_{\odot}) = 11.3$ for the galaxy (i.e. a single Sérsic-fit galaxy or a bulge plus a disk in the SerExp-fit case); but, $s_{\log R_{\text{bulge,eff}}} \approx 0.09$ at $\log_{10}(M_{\star}^{\text{Ch}}/M_{\odot}) = 10.5$ varying to ≈ 0.12 at $\log_{10}(M_{\star}^{\text{Ch}}/M_{\odot}) = 11.3$ for the bulge component in the SerExp fit. Since these errors are our formal estimates, we consider increasing them by 0.05 dex. As discussed in appendix A of Bernardi et al. (2010) the estimate of M_{\star}^{Ch} depends on the method used. Our fiducial choice is that by Bell et al. (2003) which is similar to Gallazzi et al. (2005) but gives ≈ 0.1 dex systematically larger M_{\star}^{Ch} compared with Blanton & Roweis (2007). Furthermore, stellar IMFs are not universal as described in section 2.3. Hence stellar mass is relatively more uncertain than other parameters and should be treated with caution. The aperture velocity dispersion σ_{ap} has the smallest error and is the most reliable parameter out of our measurements.

2.3 Stellar initial mass functions of ETGs

A number of recent studies (e.g., Cappellari et al. 2013b; Conroy & van Dokkum 2012; Tortora, Romanowsky & Napolitano 2013) find that the stellar IMFs for ETGs show significant galaxy-to-galaxy scatter and are in general different from the IMFs inferred for the Milky Way and other nearby galaxies (Chabrier 2003; Kroupa 2002). This means that the stellar masses derived for our galaxies using the Chabrier IMF should be corrected. Here we do not intend to describe recent IMF results comprehensively but just list some results that we use to encompass the current likely range.

The IMFs of ETGs show systematic trends with galaxy parameters such as velocity dispersion, mass-to-light ratio (M/L) and magnesium-to-iron abundance ratio [Mg/Fe]. We use the VD-dependent IMF derived by the ATLAS^{3D} project from detailed dynamical modelling of 260 nearby ETGs using observed light distributions and velocity moments (Cappellari et al. 2013a,b). The ATLAS^{3D} IMF for each galaxy corresponds to the global IMF for the galaxy (i.e. for a region of radius $\gtrsim R_{\text{eff}}$). The ATLAS^{3D} IMFs are heavier than the Chabrier and Kroupa IMFs for most range of VD and become heavier slowly with increasing VD (Fig. 2). An independent IMF distribution is obtained by detailed stellar population synthesis (SPS) modelling of the spectra of 34 nearby ETGs (Conroy & van Dokkum 2012). The SPS modelling has nothing to do with galaxy dynamics so that the result is independent of the unknown DM distribution. The SPS modelling result corresponds to the central cylindrical region of radius $R_{\text{eff}}/8$. The SPS linear relation shown in Fig. 2 is a least-square fit result based on the data including measurement errors (C. Conroy, personal communications). This result is similar to the ATLAS^{3D} result indicating that the IMF does not significantly vary radially within the galaxy. IMFs varying more rapidly than these are obtained by the SPIDER project through a combined dynamical and SPS modelling of a large number (~ 4500) of ETGs (Tortora, Romanowsky & Napolitano 2013).

Considering the agreement between the ATLAS^{3D} and the SPS results we assume that there is no radial gradient of IMF within a galaxy. We use the ATLAS^{3D} IMF distribu-

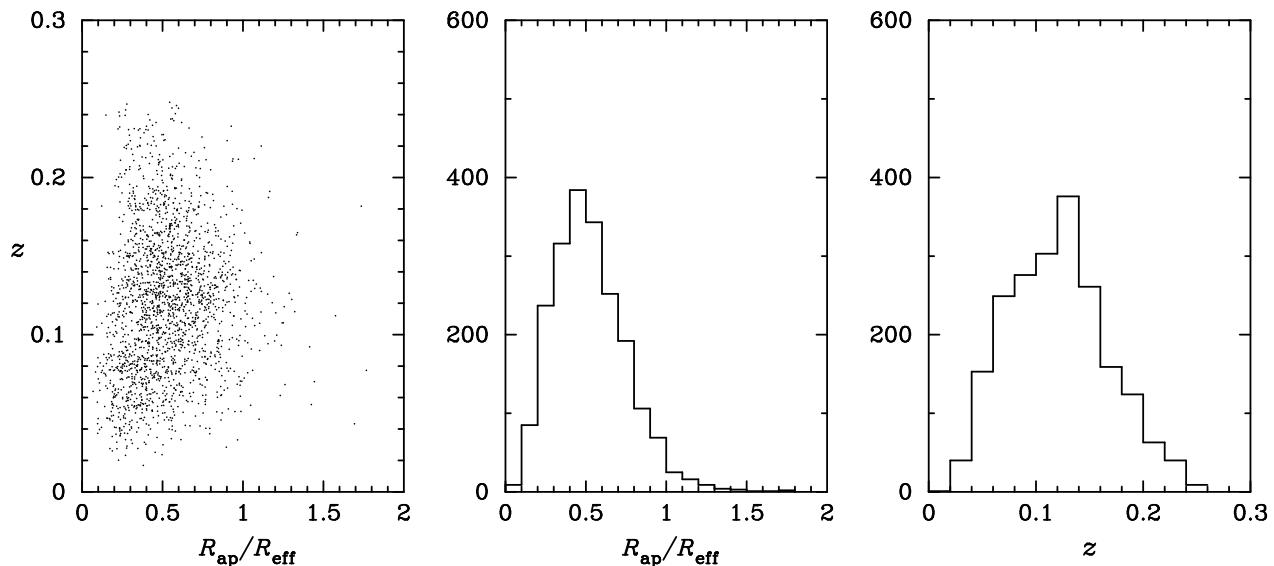


Figure 1. Distribution of $R_{\text{ap}}/R_{\text{eff}}$ (the ratio of the physical aperture radius to the effective radius) and z (redshift) in our standard sample of 2,054 nearly spherical and disk-less SDSS galaxies.

tion as our standard choice and use the others to estimate systematic errors due to IMF uncertainties.

2.4 Stellar mass–halo mass relation for ETGs

Although there are many observational and abundance matching results for the stellar mass (M_*)–halo mass (M_{200}) relation for the total population of galaxies, the results for ETGs are relatively few. We use the M_* – M_{200} relations for red galaxies or ETGs obtained by the satellite kinematics of the SDSS galaxies (More et al. 2011), weak lensing of the SDSS galaxies (Schulz, Mandelbaum & Padmanabhan 2010; Mandelbaum et al. 2006) and abundance matching of the SDSS galaxies (Chae et al. 2012) with the Bolshoi N -body simulation haloes (Klypin, Trujillo-Gomez & Primack 2011). The results from the satellite kinematics and abundance matching include intrinsic system-to-system scatter. These results are shown in Fig. 3. The satellite kinematics result is consistent with the more recent weak lensing result by Schulz, Mandelbaum & Padmanabhan (2010), while the abundance matching result with the earlier weak lensing result by Mandelbaum et al. (2006). Our standard choice is the satellite kinematics result while we use the weak lensing and abundance matching results to estimate systematic errors.

2.5 Halo mass–concentration relation

One of the current robust results from weak lensing is that the outer halo can be well described by the NFW or Einasto profile (Mandelbaum, Seljak & Hirata 2008). The scale radius or equivalently the concentration of this outer NFW/Einasto halo has been determined empirically by weak lensing but can be also predicted by cosmological N -body simulations. Our standard choice is the

weak lensing result (equation 7 and fit 2 in Table 2 of Mandelbaum, Seljak & Hirata 2008) given by

$$c_{\text{NFW}}(M_{200}) = \frac{c_0}{1+z} \left(\frac{M_{200}}{M_0} \right)^{-\nu} \quad (3)$$

with $c_0 = 5.61 \pm 0.85$, $\nu = 0.13 \pm 0.07$ and $M_0 = 10^{14} h^{-1} M_\odot$. Since some N -body simulation results can differ by $\sim 2\sigma$ from the weak lensing result, we use $\pm 2\sigma$ ($\approx \pm 30\%$) errors of the mean concentration to estimate systematic errors. Our adopted range is consistent with recent weak lensing measurements (e.g. Brimiouille et al. 2013) as well as recent N -body simulation results (e.g. Macciò et al. 2007; Duffy et al. 2008; Prada et al. 2012). We assume an intrinsic halo-to-halo scatter of 0.1 dex from the mean relation as N -body simulations predict similar scatter. Our results have little sensitivity on the precise value of the intrinsic scatter.

2.6 Line-of-sight velocity dispersion profiles for ETGs

The measured luminosity-weighted LOSVDs of ETGs can be, in most cases, well described by a simple power-law profile (see equation 12 below) in the optical region. We collect available data and do a uniform least-square-fit of LOSVD profiles. We consider the profile data for 48 nearby ETGs by Cappellari et al. (2006), the on-line data for 35 Coma cluster ETGs by Mehlert et al. (2000) and the published data for 7 BCGs at a mean redshift of $\langle z \rangle \approx 0.25$ by Newman et al. (2013). The fitted values of η (profile slope; equation 12 below) for all 90 ETGs are displayed in Fig. 4.

We note some features from Fig. 4. First, two independent samples, black points (Cappellari et al. 2006) and blue points (Mehlert et al. 2000), have indistinguishable distributions of η . Second, low VD ($\sigma_{e2} \lesssim 100 \text{ km s}^{-1}$) ETGs appear to have a higher mean of η . These low- σ_{e2} ETGs tend to have relatively less dominating bulges (M. Cappellari, per-

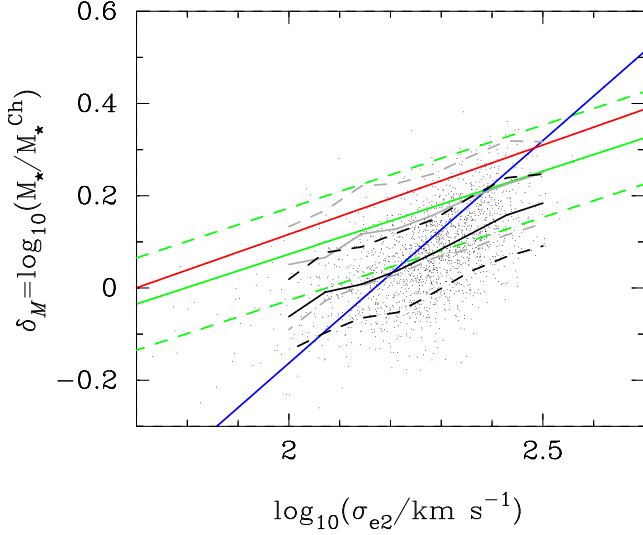


Figure 2. Stellar IMF variation as a function of σ_{e2} , aperture velocity dispersion normalized to a radius of $R_{\text{eff}}/2$. M_* is the stellar mass of the galaxy based on the σ_{e2} -dependent IMF while M_*^{Ch} is that based on the Chabrier IMF. Green solid and dashed lines are respectively the mean relation and intrinsic scatters from the ATLAS^{3D} project. The red solid line is the linear fit relation of the SPS modelling results of local ETGs while the blue solid line is an approximate median of two linear fit relations with and without modified adiabatic contraction of DM distribution from the SPIDER project. Black points and lines represent the distribution from modelling $\sim 2,000$ nearly spherical galaxies in our standard sample based on the ATLAS^{3D} input and other standard inputs (see Table 1) while gray lines represent an alternative distribution through a second modelling method for the same inputs (see section 3.3 and section 4.2.2). Note that for the literature results velocity dispersions have been converted to σ_{e2} assuming $\sigma_R \propto R^{-0.06}$.

sonal communications) meaning that they may not match well with our bulge-dominating ETGs. Third, all $z \sim 0.25$ BCGs have positive values of η (mean $\langle \eta \rangle_{\text{BCG}} \approx 0.087$) in contrast to Coma cluster cD and D galaxies NGC 4874 ($\eta = -0.0470 \pm 0.0055$), NGC 4889 ($\eta = -0.0624 \pm 0.0066$) and NGC 4839 ($\eta = -0.0068 \pm 0.0134$). The difference between the $z \sim 0.25$ BCG sample and the Coma cD/D galaxies can be largely attributed to systematic size difference and redshift evolution. The $z \sim 0.25$ BCGs have much larger sizes than the Coma cD/Ds: 5 out of the 7 BCGs have $30 \text{ kpc} \lesssim R_{\text{eff}} \lesssim 50 \text{ kpc}$ while 2 out of the 3 Coma cD/Ds have $R_{\text{eff}} < 20 \text{ kpc}$. Evolution effects cannot be neglected for the $z \sim 0.25$ clusters because of the rapid redshift evolution of massive clusters. Fourth, other than the low σ_{e2} ETG and $z \sim 0.25$ BCG peculiarities η does not vary with σ_{e2} . Finally, 8 nearly spherical ($\epsilon < 0.15$) ETGs (marked by open stars) with little rotation have a mean consistent with that for all ETGs.

Excluding the $z \sim 0.25$ BCGs, we have a mean value $\langle \eta \rangle = -0.0527 \pm 0.0045$ with an intrinsic scatter of $s_\eta = 0.0406$ for 83 ETGs and a slightly different value $\langle \eta \rangle = -0.0579 \pm 0.0039$ with $s_\eta = 0.0340$ for 77 ETGs with $\sigma_{e2} > 100 \text{ km s}^{-1}$. For the 8 nearly spherical and slowly ro-

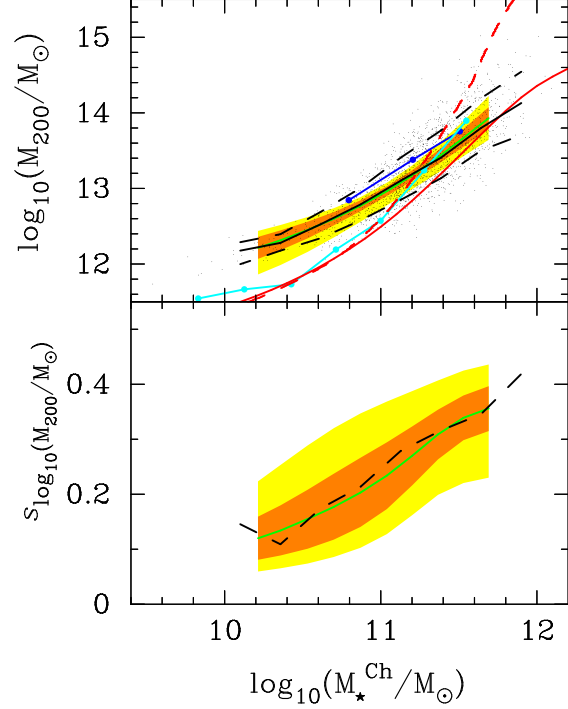


Figure 3. M_*^{Ch} - M_{200} relation and its intrinsic scatter. Orange and yellow regions show respectively the 68% and 95% confidence ranges of the mean and intrinsic scatter of $\log_{10}(M_{200}/M_\odot)$ as a function of M_*^{Ch} from satellite kinematics of SDSS ETGs (More et al. 2011). Blue and cyan curves represent the mean relations from weak lensing (Schulz et al. 2010; Mandelbaum et al. 2006). Red solid curve is the mean of M_{200} at fixed M_*^{Ch} while the red dashed curve is the mean of M_*^{Ch} at fixed M_{200} from abundance matching (Chae et al. 2012). Black points represent the distribution from modelling $\sim 2,000$ nearly spherical galaxies in our standard sample based on the satellite kinematics input and other standard inputs (see Table 1).

tating ETGs we have $\langle \eta \rangle = -0.061 \pm 0.012$ with $s_\eta = 0.031$. These values are consistent with one another. Our fiducial choice is $\langle \eta \rangle = -0.058$ with $s_\eta = 0.035$. This value is somewhat higher than the value $\langle \eta \rangle = -0.066$ by Cappellari et al. (2006) but the intrinsic scatter is identical. We take the difference between the two values (i.e. 0.008) as our estimate of the systematic error.

2.7 Velocity dispersion anisotropies

Detailed dynamical modelling results of nearby ETGs show that VD anisotropies are varying in general with r in the optical region (e.g., Gerhard et al. 2001; Thomas et al. 2007; Cappellari et al. 2007). Despite the radial variations anisotropy $\beta(r)$ (see below equation 10 and the subsequent text) values are bounded within the range $-0.9 \lesssim \beta(r) \lesssim 0.5$ for the entire radial range for most ETGs. For the case of using constant anisotropies we use an asymmetric pseudo-Gaussian probability density distribution given by

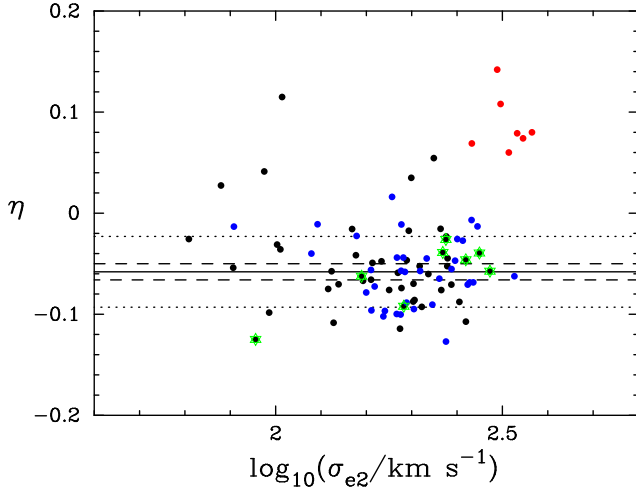


Figure 4. Distribution of velocity dispersion profile slope η (equation 11) of published nearby ETGs. Black points are field and cluster ETGs from Cappellari et al. (2006) while blue points are ETG members of the Coma cluster (Mehlert et al. 2000). Green open stars represent nearly spherical galaxies with little rotation. Red points are BCGs at $z \sim 0.25$ by Newman et al. (2013). Black solid line is the mean of the black and blue data points with $\log_{10}(\sigma_{e2}/\text{km s}^{-1}) > 2$. Dashed lines represent our adopted systematic errors of the mean while dotted lines represent intrinsic scatters of the distribution.

$$P(\beta) = \frac{1}{\sqrt{\pi/2}(s_L + s_H)} \times \begin{cases} \exp\left[-\frac{(\beta - \mu_\beta)^2}{2s_L^2}\right] & (\beta < \mu_\beta) \\ \exp\left[-\frac{(\beta - \mu_\beta)^2}{2s_H^2}\right] & (\beta \geq \mu_\beta) \end{cases} \quad (4)$$

with $\mu_\beta = 0.18$ (peak value), $s_H = 0.11$ (higher value dispersion) and $s_L = 0.25$ (lower value dispersion) derived by Chae et al. (2012) using 40 unoverlapping ETGs in the literature. The distribution has a mean of $\langle\beta\rangle = 0.056$. We take this constant value distribution as our fiducial choice.

As a way of estimating systematic effects of radially varying anisotropies we use a smoothly varying function of the form (appendix B, Chae et al. 2012)

$$\beta(r) = \beta_0 + \beta_1 \frac{r^2}{r^2 + r_1^2} + \beta_2 \frac{r^2}{r^2 + r_2^2} \quad (5)$$

with the central anisotropy $-0.3 < \beta_0 < 0.3$, $0 < r_1, r_2 < R_{\text{eff}}$, mean anisotropy within R_{eff} taking the distribution of equation (4), and the anisotropy at large radii $0 < \beta_\infty < 0.3$ motivated from N-body simulations (e.g. Navarro et al. 2010).

2.8 The centres of early-type galaxies

While the main bodies of ETGs can be well described by the Sérsic (or SerExp) model, the central sub-kiloparsec regions are known to deviate from the the Sérsic extrapolation (e.g., Faber et al. 1997; Rest et al. 2001; Hyde et al. 2008; Kormendy et al. 2009; Glass et al. 2011). There can be missing or extra light compared with the Sérsic extrapolation of the bulge component (or the galaxy) depending on the nature of the galaxy. The galaxies with missing central light are mostly giant ETGs (sometimes referred to as the core

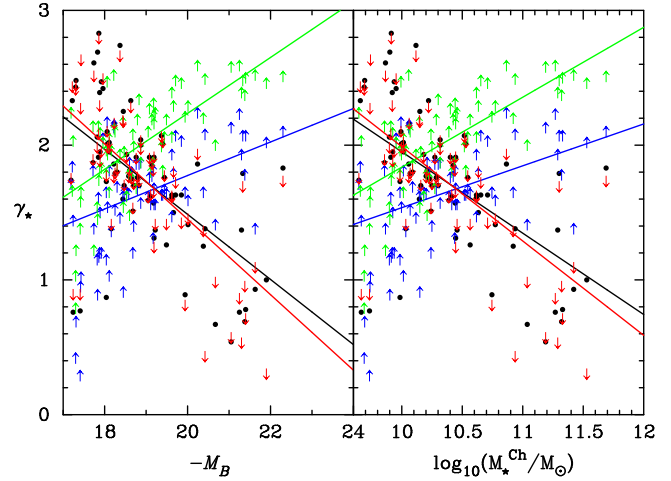


Figure 5. Measured values of the three-dimensional luminosity (stellar mass) density slope γ_* ($\equiv -d \ln \rho_*(r)/d \ln r$) at four different radii, $0.005R_{\text{eff}}$ (red symbols), $0.01R_{\text{eff}}$ (black), $0.05R_{\text{eff}}$ (blue) and $0.3R_{\text{eff}}$ (green) for 79 ETGs ($M_B < -17$) imaged with the *Hubble Space Telescope* ACS (Glass et al. 2011). In the right-hand side panel M_*^{Ch} is the stellar mass based on the Chabrier IMF using a photometric conversion described in the text.

galaxies), while those with extra central light are less luminous ETGs (sometimes referred to as the power-law galaxies). On average, core galaxies have much shallower central slopes compared with power-law galaxies.

Recent detailed *Hubble Space Telescope* observations of the centres of ETGs for a wide range of luminosities show that the central slope varies systematically with luminosity (Glass et al. 2011; Rest et al. 2001). Furthermore, the central slope varies radially in the central region of a galaxy. Fig. 5 shows three-dimensional central slope γ_* ($\equiv -d \ln \rho_*(r)/d \ln r$) values at four different radii, $0.005R_{\text{eff}}$, $0.01R_{\text{eff}}$, $0.05R_{\text{eff}}$ and $0.3R_{\text{eff}}$ for 79 ETGs with $M_B < -17$ (Glass et al. 2011), or $\log_{10}(M_*^{\text{Ch}}/M_\odot) \gtrsim 9.6$ using $\log_{10}(M_*^{\text{Ch}}/M_\odot) = 1.097(g-r) - 0.406 - 0.4(M_r - 4.67)$, $g-r \sim 0.75$ (Bernardi et al. 2010) and $B = g + 0.313(g-r) + 0.227$ (Lupton 2005). The slope at $r = 0.01R_{\text{eff}}$ scales as $\gamma_{0.01} = 1.34 - 0.603(\log_{10}(M_*^{\text{Ch}}/M_\odot) - 11)$ (black line in Fig. 5).

The break radius at which the luminosity profile starts to deviate from the main-body Sérsic profile is typically $r_b \approx 0.03R_{\text{eff}}$ (Faber et al. 1997) but varies systematically from $\sim 0.01R_{\text{eff}}$ up to $\sim 0.3R_{\text{eff}}$ according to a more recent study by Kormendy et al. (2009). Fig. 6 shows a systematic trend of r_b/R_{eff} based on 21 ETGs of the Virgo cluster brighter than $M_V = -18$ (Kormendy et al. 2009). Stellar mass M_*^{Ch} for each galaxy is obtained using a photometric conversion $V = g - 0.5784 \times (g-r) - 0.0038$ (Lupton 2005). We obtain a least-square fit relation $\log_{10}(r_b/R_{\text{eff}}) = a + b \log_{10}(M_*^{\text{Ch}}/M_\odot)$ with $a = 4.6577 \pm 0.0903$ and $b = -0.5502 \pm 0.0088$.

The central missing or extra light cannot affect significantly our modelling results for the mass profile outside the central region. Nevertheless, we take into account the central light distribution as follows to obtain as accurate as possible results particularly for the central region. We assume a

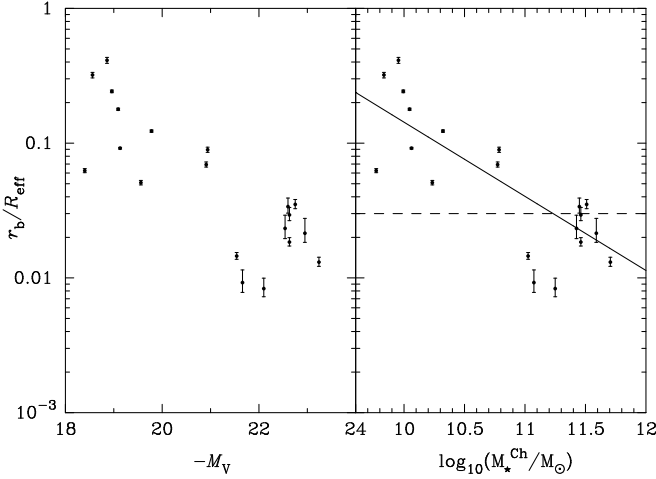


Figure 6. Measured values of break radius r_b normalized by R_{eff} for 21 ETGs of the Virgo cluster brighter than $M_V = -18$ based on a wealth of data taken with a number of telescopes including the *Hubble Space Telescope* (Kormendy et al. 2009). Here each value of r_b is defined to be the minimum radius of the main-body Sérsic fit except for NGC 4459 whose minimum radius was reread from its light profile.

linearly varying slope $\gamma(r) = \gamma_0 + m(r/R_{\text{eff}})$ with the corresponding density $\rho_*(r) = \rho_0(r/R_{\text{eff}})^{-\gamma_0} \exp[-m(r/R_{\text{eff}})]$ for $r < r_b$. For each galaxy in our sample we determine γ_0 and m by requiring that the slope is continuous with the Sérsic slope at r_b and the slope at $r = 0.01R_{\text{eff}}$ matches the empirical mean value $\gamma_{0.01}$ given above. Our fiducial choice for r_b is $0.03R_{\text{eff}}$. To estimate systematic errors we consider alternatively the varying r_b shown in Fig. 6.

3 MASS MODELS AND JEANS ANALYSIS

We use the spherical Jeans equation (see section 3.2) to constrain galactic mass profiles of nearly spherical galaxies in our sample. We take parametric approach and consider for the total mass distribution single-component and two-component models. Two-component models are clearly more realistic and better-motivated because observed elliptical galaxies are believed to have at least two separate components (i.e. luminous and DM components). In single-component models the unknown DM component is treated implicitly. Single-component models are considered because they can provide qualitatively different profiles and thus can allow useful comparison with two-component models.

3.1 Parametric models of mass distribution

In two-component models the total mass distribution results from the superposition of the empirically derived stellar mass distribution and the unknown DM distribution (gas mass is negligible for our ellipticals), namely

$$\rho(r) = \rho_*(r) + \rho_{\text{DM}}(r). \quad (6)$$

We assume that the DM profile varies smoothly from the inner to the outer halo. Specifically, we consider two classes of profiles for DM distribution.

One is the generalized NFW (gNFW) model given by

$$\rho_{\text{gNFW}}(r) = \frac{\rho_s}{(r/r_s)^\alpha (1 + r/r_s)^{3-\alpha}}, \quad (7)$$

where α is the limiting slope as $r \rightarrow 0$, and ρ_s and r_s are related to the concentration parameter c ($\equiv r_{200}/r_s$) and M_{200} (Chae et al. 2012).

The other is the Einasto model (Einasto & Haud 1989) given by

$$\rho_{\text{Einasto}}(r) = \rho_{-2} \exp \left\{ -(2/\tilde{\alpha}) \left[(r/r_{-2})^{\tilde{\alpha}} - 1 \right] \right\}, \quad (8)$$

where r_{-2} (the radius at which the logarithmic slope of the density is -2) and ρ_{-2} are similarly related to c_{-2} ($\equiv r_{200}/r_{-2}$) and M_{200} (Chae et al. 2012).

For the single-component case we consider for the total mass distribution the gNFW model (equation 7) and a simple power-law model given by

$$\rho_{\text{PL}}(r) = \rho_0 \left(\frac{r}{r_0} \right)^{-\gamma_{\text{PL}}}, \quad (9)$$

where ρ_0 is the density at a fiducial radius r_0 . This constant slope model (equation 9) is not intended to describe mass profile at large radii but just the profile in the optical region.

3.2 Spherical Jeans equation and velocity dispersion

For the total mass profile $M(r) = M_*(r) + M_{\text{DM}}(r)$ we use the spherical Jeans equation (Binney & Tremaine 2008) given by

$$\frac{d[\rho_*(r)\sigma_r^2(r)]}{dr} + 2\frac{\beta(r)}{r}[\rho_*(r)\sigma_r^2(r)] = -G\frac{\rho_*(r)M(r)}{r^2}, \quad (10)$$

where $\sigma_r(r)$ is the radial stellar velocity dispersion at radius r and $\beta(r)$ is the velocity dispersion anisotropy at r given by $\beta(r) = 1 - \sigma_t^2(r)/\sigma_r^2(r)$ where $\sigma_t(r)$ is the tangential velocity dispersion in spherical coordinates. An integral solution of the Jeans equation for $\sigma_r(r)$ with the general form of $\beta(r)$ given by equation (5) can be found in Chae et al. (2012).

The LOSVD of stars at projected radius R on the sky $\sigma_{\text{los}}(R)$ is given by (Binney & Mamon 1982)

$$\sigma_{\text{los}}^2(R) = \frac{1}{\Sigma_*(R)} \int_{R^2}^{\infty} \rho_*(r)\sigma_r^2(r) \left[1 - \frac{R^2}{r^2}\beta(r) \right] \frac{dr^2}{\sqrt{r^2 - R^2}}, \quad (11)$$

where $\Sigma_*(R)$ is the two-dimensional stellar mass density projected on the sky. Observed ETGs show that the luminosity weighted LOSVD within an aperture of radius R is, in most cases, well-described by a power-law profile (Cappellari et al. 2006; Mehlert et al. 2000), i.e.,

$$\begin{aligned} \sigma_R \equiv \langle \sigma_{\text{los}} \rangle(R) &= \frac{\int_0^R \Sigma_*(R')\sigma_{\text{los}}(R')R'dR'}{\int_0^R \Sigma_*(R')R'dR'} \\ &= \sigma_{e2} \left(\frac{R}{R_{\text{eff}}/2} \right)^\eta, \end{aligned} \quad (12)$$

where σ_{e2} is the velocity dispersion within the fiducial radius of $R_{\text{eff}}/2$, which on average corresponds to the aperture radius for the SDSS galaxies in our sample (see Fig. 1).

Table 1. Summary of the standard inputs

item	description	reference
galaxy sample	2,054 galaxies with $\varepsilon < 0.15$ & $\log_{10}(R_{\text{eff}}^a/R_{\text{bulge,eff}}^b) < 0.19$	this work
stellar IMF distribution	ATLAS ^{3D}	Cappellari et al. (2013b)
$M_{\star}^{\text{Ch}}-M_{200}$ relation	satellite kinematics	More et al. (2011)
$M_{200} - c_{\text{NFW}}$ relation for $r > 0.2r_{200}$	weak lensing relation equation (3) with intrinsic scatter of 0.1dex	Mandelbaum, Seljak & Hirata (2008)
VD profile	$\langle \eta \rangle = -0.058$, $\sigma_{\eta} = 0.035$	derived from the literature
VD anisotropy	asymmetric pseudo – Gaussian distribution ($\mu_{\beta} = 0.18$, $\sigma_{\text{H}} = 0.11$, $\sigma_{\text{L}} = 0.25$) of constant β (equation 4)	derived from the literature
break (core) radius	$r_b = 0.03R_{\text{eff}}$	Faber et al. (1997)
DM distribution model	gNFW	generic (equation 7)

^a The effective radius of the total light in the single Sérsic fit.

^b The effective radius of the bulge component in the SerExp fit.

3.3 Procedures of constructing a model set

For each galaxy in our sample the only direct dynamical constraint is the aperture velocity dispersion σ_{ap} . Additionally, we have the statistical distribution of velocity dispersion profile slopes within R_{eff} (section 2.6) and the statistical information of the halo virial mass M_{200} (section 2.4) and its profile at $r > 0.2r_{200}$ (section 2.5). The procedure of constructing a model set for our galaxy sample is not unique but depends on how to treat these direct and indirect constraints. We consider two approaches.

In the first approach, to be called “step-by-step approach”, we produce a degenerate parameter set of a given mass model that are solutions of the spherical Jeans equation for σ_{ap} . Then, we use the indirect constraints to break the degeneracy and test the model set statistically. In this approach σ_{ap} , the most reliable dynamical information, is reproduced without any bias.

In the second approach (to be called “chi-square approach”), we try to fit simultaneously all direct and indirect constraints by defining a goodness-of-fit χ^2 taking into account all available measurement errors and intrinsic scatterers. In this approach all direct and indirect dynamical constraints are treated equally. However, it does not guarantee that σ_{ap} is reproduced without bias. For this reason our standard approach will be the step-by-step approach. We describe in detail the two procedures in turn.

3.3.1 Step-by-step approach

(i) Each galaxy has the stellar mass M_{\star}^{Ch} based on the Chabrier IMF and Sérsic parameters fitted to the surface brightness data. A three-dimensional stellar mass profile is obtained by de-projecting the Sérsic surface brightness profile assuming the constant Chabrier IMF.

(ii) (a) We assign M_{\star} by drawing a value of $\delta_M \equiv \log_{10}(M_{\star}/M_{\star}^{\text{Ch}})$ randomly from an empirical distribution of IMF as a function of velocity dispersion as described in sec-

tion 2.3. (b) We assign a halo mass M_{200} using an empirical stellar-to-halo mass relation (section 2.4) and an NFW concentration c_{NFW} for $r > 0.2r_{200}$ using weak lensing derived $c_{\text{NFW}}-M_{200}$ relation (section 2.5). (c) We also assign a VD anisotropy $\beta(r)$ from an empirical distribution (section 2.7).

(iii) For the above assignment of δ_M , M_{200} , c_{NFW} and $\beta(r)$ to the galaxy we produce a degenerate parameter set $\{\alpha, c\}$ with the prior $0 < \alpha < 3$ for the gNFW (equation 7) or $\{\tilde{\alpha}, c_{-2}\}$ with the prior $0 < \tilde{\alpha} < 0.9$ for the Einasto (equation 8) by requiring that each set reproduces σ_{ap} . In some cases the assigned random parameter combinations from step (ii) may not allow any solution for σ_{ap} . In those cases we go back to step (ii) and re-assign parameters. For about 10 percent of galaxies solutions are not found through a significant number of iterations. We reject those galaxies in this approach. In this random process the posterior distribution of any parameter may be readjusted from the prior input distribution as required by the aperture velocity dispersion. We allow this readjustment to happen because the aperture velocity dispersion is more reliable than those empirical inputs used in step (ii). For the case of the power-law model (equation 9) for the total mass distribution we have two free parameters γ_{PL} and ρ_0 but we fix ρ_0 by requiring that near the galactic centre the total mass density is equivalent to the stellar mass density to a good approximation. So, in this case the only free parameter γ_{PL} is uniquely determined by σ_{ap} .

(iv) Out of the degenerate set from step (iii) we select a model that best matches the weak lensing constraint by minimizing the following

$$\Delta^2 = \sum_i \left(\frac{\log \rho^{\text{mod}}(r_i) - \log \rho^{\text{WL}}(r_i)}{s_{\log \rho(r_i)}} \right)^2, \quad (13)$$

where $0.2r_{200} < r_i < r_{200}$, $\rho^{\text{mod}}(r_i)$ is the model density, $\rho^{\text{WL}}(r_i)$ is the density from the weak lensing NFW-fit concentration (section 2.5) for the given halo mass, and $s_{\log \rho(r_i)}$ is the error associated with the scatter of 0.1 dex in c_{NFW} .

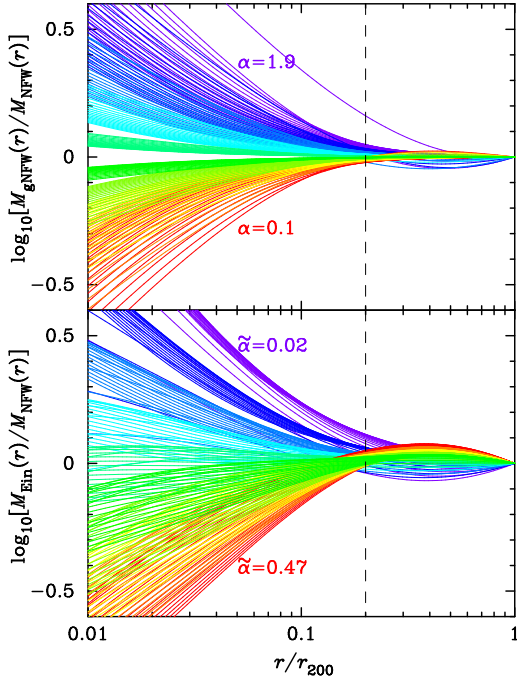


Figure 7. The DM mass profiles relative to the NFW profile with the outer halo ($r > 0.2r_{200}$) profile constraints (equation 14 & equation 15) imposed. Each coloured set of curves are for a specific value of α for the gNFW or $\tilde{\alpha}$ for the Einasto. Different curves in the set correspond to different values of c_{NFW} from the range $2 \leq c_{\text{NFW}} \leq 29$. In the outer halo region the deviation of the gNFW mass $M_{\text{gNFW}}(r)$ from the NFW mass $M_{\text{NFW}}(r)$ is less than 0.05 dex for almost all occurrences and less than 0.02 dex for most likely occurrences. The deviation of the Einasto mass $M_{\text{Ein}}(r)$ can be up to 0.1 dex but is less than 0.05 dex for most likely occurrences.

(v) Finally, we calculate the slope of σ_R profile, η (equation 12), for the selected model from step (iv) using a least-square fit between $0.1R_{\text{eff}}$ and R_{eff} . We then compare the distribution of η for the galaxy sample with the observed distribution (Fig. 4, section 2.6) to test the mass model being considered.

The above procedures (iii) and (iv) can be simplified by noting that the minimization of equation (13) is, to a good approximation, equivalent to a constraint relation between α and c (or, between $\tilde{\alpha}$ and c_{-2}) for the assigned value of c_{NFW} for $r > 0.2r_{200}$. Such a constraint relation can be obtained in several ways but most easily by requiring that the slope of the DM profile matches that of the NFW profile at an optimal radius r_0 .

The constraint relation for the gNFW profile is

$$c = \max \left[\left(\frac{3 - \alpha}{2} c_{\text{NFW}} + \frac{1 - \alpha}{2} \frac{r_{200}}{r_0} \right), \delta \right], \quad (14)$$

where δ is an arbitrarily small positive number ensuring that c is positive, and that for the Einasto profile is

$$c_{-2} = \frac{r_{200}}{r_0} \left[\frac{3}{2} - \frac{1}{1 + c_{\text{NFW}} r_0 / r_{200}} \right]^{1/\tilde{\alpha}}. \quad (15)$$

From numerical experiments we select $r_0 = (2/9)r_{200}$.

Fig. 7 shows the gNFW/Einasto mass profiles relative

to the NFW profile with the outer profile constraints (equation 14 & equation 15) imposed. We consider $2 \leq c_{\text{NFW}} \leq 29$ to fully cover the empirical range. We then consider the plausible posterior range $0.1 \leq \alpha \leq 1.9$ for the gNFW and $0.02 \leq \tilde{\alpha} \leq 0.47$ for the Einasto. For virtually all plausible combinations of c_{NFW} and α the gNFW profile deviates from the NFW by less than 0.05 dex for $0.2r_{200} \leq r \leq r_{200}$. For the Einasto profile the deviation can be as large as ≈ 0.1 dex but for the most likely combinations it is less than 0.05 dex.

With the constraint relation (equation 14 or 15) the effective number of free parameters is just one. We choose one free parameter to be α (or, $\tilde{\alpha}$). Notice that by varying the free parameter of the assumed DM model baryonic effects in the inner halo (Gnedin et al. 2004; Sellwood & McGaugh 2005; Gnedin et al. 2011), if present, can be taken into account.

3.3.2 chi-square approach

In this approach we intend to fit all three dynamical constraints (i.e. σ_{ap} , the statistical distribution of η , and the statistical distribution of c_{NFW} for $r > 0.2r_{200}$) simultaneously by defining a suitable χ^2 . The power-law model (equation 9) is not applicable for this approach because it cannot simultaneously satisfy both stellar kinematics and weak lensing constraints. We first note that we can use the constraint relation (equation 14 or 15) to reduce one term in χ^2 . We have verified that including a term like equation (13) is equivalent to using the constraint. Hence there remains just one free parameter α (or $\tilde{\alpha}$) and we define the following goodness-of-fit statistic

$$\chi^2 = \chi_V^2 + \chi_\eta^2 \quad (16)$$

where $\chi_x^2 = (x^{\text{mod}} - x^{\text{emp}})^2 / s_x^2$ for $V = \log_{10}(\sigma/\text{km s}^{-1})$ and η (equation 12) with x^{mod} and x^{emp} are the theoretical model and empirical (observational) values and s_x is the error contributed by the measurement error for x^{emp} and/or the error for x^{mod} due to the measurement errors of M_\star and R_{eff} as described in section 2.2.

The first term in equation (16) is

$$\chi_V^2 = \frac{[V^{\text{mod}}(\alpha; \vec{p}) - V^{\text{emp}}]^2}{s_V^2}, \quad (17)$$

where V^{emp} is the measured value and \vec{p} includes the empirical input parameters. The dispersion s_V^2 is

$$s_V^2 = s_{V,\text{meas}}^2 + \delta V^2(s_{\log R_{\text{eff}}}) + \delta V^2(s_{\log M_\star}) \quad (18)$$

where $s_{V,\text{meas}}$ is the measurement error and $\delta V(s_{\log R_{\text{eff}}})$ and $\delta V(s_{\log M_\star})$ are the errors in V^{mod} respectively due to $s_{\log R_{\text{eff}}}$ and $s_{\log M_\star}$ (the measurement errors of $\log R_{\text{eff}}$ and $\log M_\star$).

The second term in equation (16) is

$$\chi_\eta^2 = \frac{[\eta^{\text{mod}}(\alpha; \vec{p}) - \eta^{\text{emp}}]^2}{s_\eta^2}, \quad (19)$$

where η^{emp} is a value assigned empirically (section 2.6). The dispersion s_η^2 is

$$s_\eta^2 = \delta \eta^2(s_{\log R_{\text{eff}}}) + \delta \eta^2(s_{\log M_\star}) \quad (20)$$

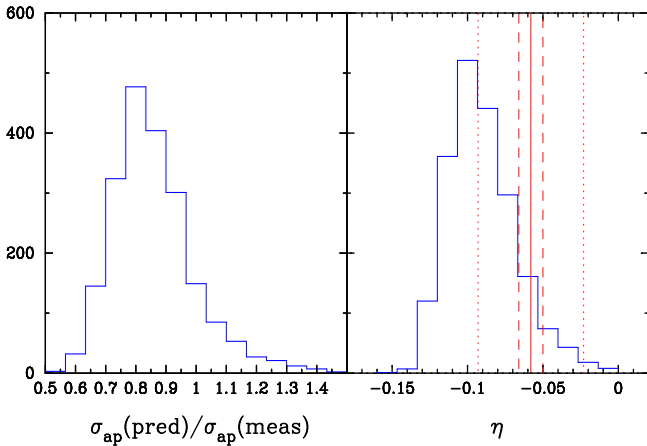


Figure 8. The predicted aperture velocity dispersion σ_{ap} and velocity dispersion profile slope η (equation 12) for the pure stellar mass profiles of 2,054 nearly spherical galaxies in our standard sample based on the constant Chabrier IMF. The predicted σ_{ap} is systematically lower than the measured value while the predicted η is systematically steeper than the measured distribution indicated by vertical red lines as shown in Fig. 4.

where $\delta\eta(s_{\log R_{\text{eff}}})$ and $\delta\eta(s_{\log M_{\star}})$ are the errors in η^{mod} respectively due to $s_{\log R_{\text{eff}}}$ and $s_{\log M_{\star}}$ (the measurement errors of $\log R_{\text{eff}}$ and $\log M_{\star}$).

We minimize the χ^2 over α coupled with c (or, $\tilde{\alpha}$ coupled with c_{-2}) with the assigned values of the empirical parameters as in step (ii) of section 3.2.1. In minimizing the χ^2 we impose the following prior constraints $0 < \alpha < 3$ (or, $0 < \tilde{\alpha} < 0.9$). For most cases, the χ^2 has a well-defined minimum within these prior constraints for the assigned values of the input parameters. If the minimum value of χ^2 has $\chi_{\text{min}}^2 > 9$ or the minimum point tries to cross the boundary of the prior constraint, we retry by selecting other random values of the input parameters from the empirical ranges.

4 RESULTS

4.1 The case of pure stellar mass distribution based on constant IMF

We first consider the case without any modelling. In this case the total mass distribution is just the stellar mass distribution based on the constant Chabrier IMF. Fig. 8 shows the predicted aperture velocity dispersion σ_{ap} and the velocity dispersion profile slope η for $0.1R_{\text{eff}} < R < R_{\text{eff}}$ based on the distribution of constant anisotropies given by equation (4). We notice that the predicted σ_{ap} is lower and the predicted η is steeper than measured. The lower σ_{ap} can, in principle, be remedied using heavier IMFs than the Chabrier, although this statement is uncertain due to the large systematic error in estimates of stellar mass even for a fixed IMF (see section 2.2). However, the steeper η can only be remedied by including another mass component whose relative contribution increases with radius. The implied mass component is of course dark matter.

4.2 Jeans modelling results

Each galaxy has not only directly measured parameters such as M_{\star}^{Ch} , R_{eff} , n and σ_{ap} but also indirectly assigned parameters such as δ_M , M_{200} , c_{NFW} and additionally η for the chi-square approach. The fitted mass profile for each galaxy depends then on the specific set of values of the indirectly assigned parameters. The specific set can be regarded as a member of the empirical ensemble or multi-dimensional space of the parameters. For each galaxy there exists an ensemble of models corresponding to the empirical parameter ensemble. This means that a run of modelling for the given sample of N galaxies produces a set of N models, each of which is a random member of the respective ensemble of models. Another run produces different members for the respective galaxies but the statistical properties of the sample remain the same. In this sense only the statistical results of the sample are meaningful from our modelling. However, variations of the empirical inputs can change the N model ensembles and accordingly the statistical results as discussed in section 5 below.

In this section we present our results based on the standard (fiducial) inputs summarized in Table 1. The results based on other systematically varied inputs will be considered in section 5. We first present the results for the single-component models (section 4.2.1) and then for the two-component models (section 4.2.2).

4.2.1 Results for the single-component models

For the single-component case we consider only the step-by-step approach because the dispersion s_{η}^2 (equation 20) is not well-defined. Since there will be no bias in the predicted σ_{ap} by the step-by-step approach, our primary test will be the distribution of η . We are considering two models for the total mass distribution, the gNFW model (equation 7) and the power-law model (equation 9).

Due to the lack of flexibility of the single-component model the predicted total mass density can be lower than the stellar mass density near the galactic center. This problem cannot be avoided particularly for the gNFW model. The constrained gNFW mass density becomes lower than the input stellar mass density at $R \lesssim R_{\text{eff}}/3$. We can remedy this by considering a two-component model explicitly including the stellar mass profile as will be done in section 4.2.2.

The power-law model is intended only as a local model for the optical region because its constant slope cannot simultaneously describe the optical region and the halo at large radii. So, in this case we use one remaining freedom to fix the total density near the centre to match the input stellar density.

The predicted distributions of η and $\gamma \equiv -\ln \rho(r)/d \ln r$ can be found in Fig. 9. These slopes are the least-square fit values between $0.1R_{\text{eff}}$ and R_{eff} . The predicted η distributions are clearly discrepant with the observed distribution and consequently the predicted γ distributions are not reliable. The gNFW model predicts too shallow η implying that the monotonic radial density slope variation in the model produces an artefact when the model is constrained by the aperture velocity dispersion at small radii and by the weak lensing constraint at large radii. The large scatter in η in addition to the biased mean for the power-law model indi-

Figure 9. The predicted velocity dispersion profile slope η (equation 12) and density slope γ between $0.1R_{\text{eff}}$ and R_{eff} for the single-component PL (equation 9) and gNFW (equation 7) models for the total mass distribution. The measured distribution of η is indicated by vertical red lines as shown in Fig. 4. The arrows indicate the mean values.

cates that the model without a proper profile at large radii is ill constrained by the aperture velocity dispersion alone. We will see in section 4.2.2 that the problems of the single-component models are naturally removed when we consider more realistic two-component models. The single-component models will not be considered any further.

4.2.2 Results for the two-component models

Fig. 10 shows the predicted distribution of η for the two-component model based on the standard inputs (Table 1). Its mean, median and RMS scatter are -0.052 , -0.054 and 0.028 by the step-by-step approach and -0.059 , -0.060 and 0.022 by the chi-square approach. The mean and median values agree well with the observationally inferred mean $\langle\eta\rangle = -0.058 \pm 0.008$. The predicted scatter is somewhat smaller than the observed scatter $s_\eta = 0.035$. We show in section 5 that we can produce the observed scatter or even larger scatters by including galaxies of larger ellipticities or lower concentrations or by considering radially varying anisotropies. For the case of the chi-square approach the predicted aperture velocity dispersion is on average 0.05 dex higher than measured (larger than the measurement error of 0.04 dex) while there is no such bias for the step-by-step approach.

Fig. 2 shows the predicted distribution of IMF variation $\delta_M [= \log_{10}(M_*/M_*^{\text{Ch}})]$. The predicted slope of the variation is within the current empirical range. The magnitude of δ_M by the step-by-step approach is lower than the input ATLAS^{3D} value (Cappellari et al. 2013b) but is overall consistent with the SPIDER (Tortora, Romanowsky & Napolitano 2013) value. Note that the magnitude of δ_M depends also on M_*^{Ch} which suffers from its own uncertainty (see section 2.2). This means that the shift of δ_M from the input is not likely to be a problem. The magnitude of δ_M by the chi-square approach agrees well with the input ATLAS^{3D} IMF for the sake of the biased prediction on σ_{ap} as mentioned above.

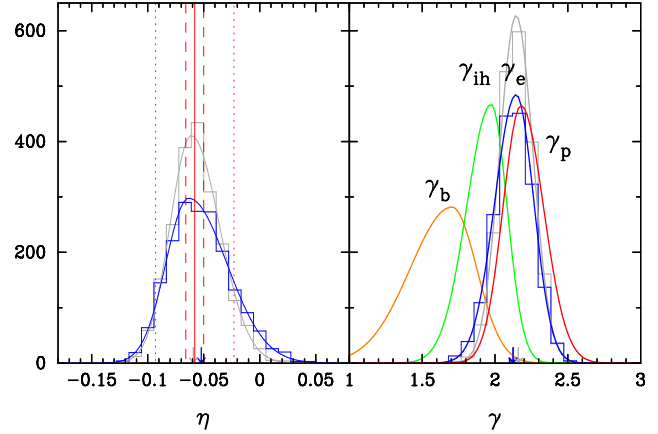


Figure 10. (Left) The predicted velocity dispersion profile slope η (equation 12) between $0.1R_{\text{eff}}$ and R_{eff} for the two-component model with the gNFW (equation 7) DM component with the standard inputs (Table 1). The blue result is by the step-by-step approach while the gray result is by the chi-square approach. The measured distribution of η is indicated by vertical red lines as shown in Fig. 4. (Right) The predicted density slopes for the model shown left. γ_e is the least-square fit slope between $0.1R_{\text{eff}}$ and R_{eff} while γ_{ih} is between $0.1R_{\text{eff}}$ and $0.1r_{200}$. γ_p and γ_b correspond respectively to the peak turning point and the bottom (trough) turning point in a global S-shape of the slope function.

Fig. 3 shows that the posterior distribution of M_{200} as a function of M_*^{Ch} is consistent with the input relation and scatter.

For the result based on the step-by-step approach Fig. 10 shows the predicted distributions of variously defined density slopes γ_e , γ_{ih} , γ_p and γ_b , which are considered for curvatures in the predicted slope function. γ_e is the least-square fit slope in the optical region between $0.1R_{\text{eff}}$ and R_{eff} while γ_{ih} is for an inner halo region between $0.1R_{\text{eff}}$ and $0.1r_{200}$. As shown in Fig. 11 and Fig. 12 and described below, the predicted slope function is usually curved to have two stationary (turning) points. γ_p and γ_b correspond to the values respectively at the peak and the bottom (trough) turning points. The predicted mean and RMS scatter of γ_e are $\langle\gamma_e\rangle \approx 2.12$ and $s_{\gamma_e} \approx 0.14$ ($\langle\gamma_e\rangle \approx 2.16$ and $s_{\gamma_e} \approx 0.11$ for the chi-square approach), which are steeper than isothermal.

Fig. 11 shows the total mass density profile $\rho(r)$ and the density slope profile $\gamma(r)$ for 16 galaxies randomly selected from our sample in comparison to the published density profiles of 16 Coma cluster ETGs based on detailed dynamical modelling by Thomas et al. (2007) (see also Fig. 14 of Thomas et al. 2011). There is a reasonable agreement (within 2σ) between the two samples. There is a significant galaxy-to-galaxy scatter in the individual profiles but a systematic pattern in $\gamma(r)$ emerges independently from both samples. Typically, there is a $\gamma > 2$ (steeper than isothermal) region within the optical region at $r < 10$ kpc, surrounded by a $\gamma < 2$ (shallower than isothermal) region within the inner halo ($r < 0.1r_{\text{vir}}$), which is then surrounded by a $\gamma > 2$ outer halo.

Fig. 12 shows the average profiles $\rho(r)$ and $\gamma(r)$ for 6 sub-samples defined by halo mass M_{200} . Each subsample has

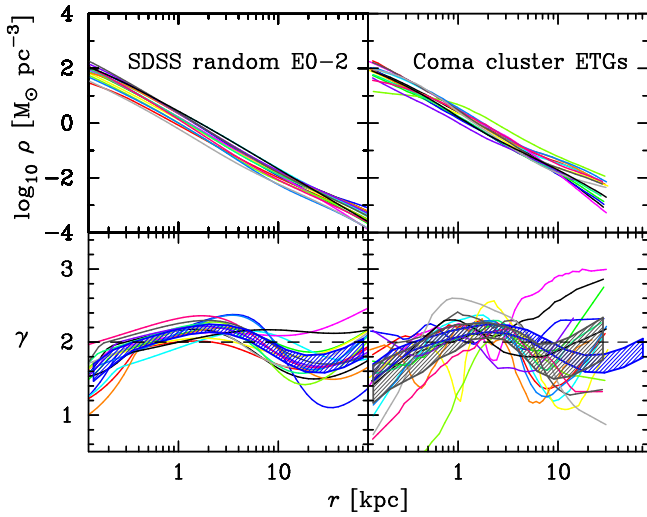


Figure 11. The left-hand side displays the radial total (stellar plus dark) mass density profiles for randomly selected 16 SDSS nearly spherical galaxies ($b/a > 0.85$) and their negative slope profiles $\gamma = -d \log \rho / d \log r$. The blue hatched region shows the 2σ uncertainty of the sample mean. On the right-hand side the published density profiles (Thomas et al. 2007) for 16 Coma cluster ETGs (with profiles extending beyond R_{eff}) are compared with our ellipticals. The dark hatched region shows the 2σ uncertainty of the sample mean for Coma cluster ETGs.

a range of ± 0.2 dex in $\log_{10} M_{200}$. This figure reveals more precisely and in greater detail the behaviours of $\rho(r)$ and $\gamma(r)$ already indicated in Fig. 11. The average profile $\rho(r)$ in the optical region ($r < R_{\text{eff}}$) is steeper than isothermal with $\gamma \approx 2.1 - 2.2$ for most sub-samples. The optical region has a super-isothermal peak of γ which is surrounded by a sub-isothermal valley in the inner halo ($r < 0.1r_{200}$). This valley is due to the increased contribution from dark matter at larger radii. The isothermal crossing from the super-isothermal peak to the sub-isothermal valley occurs at $r_{\text{pb}} \approx R_{\text{eff}}$ for $M_{200} = 10^{13.5} M_{\odot}$, $R_{\text{eff}} < r_{\text{pb}} < 2R_{\text{eff}}$ for $M_{200} < 10^{13.5} M_{\odot}$, and $0.5R_{\text{eff}} < r_{\text{pb}} < R_{\text{eff}}$ for $M_{200} > 10^{13.5} M_{\odot}$. Interestingly, if a constant slope profile were used to fit the entire inner halo region ($0 < r < 0.1r_{200}$), the best-fit profile would be close to isothermal for $M_{200} \lesssim 10^{13.5} M_{\odot}$. Hence the isothermal model can be valid only as a first order approximation to the entire inner halo region of galaxies but generally is not an accurate representation of the real profile.

Fig. 13 shows the distribution of four characteristic slopes against various parameters. As indicated by the points for γ_e , there is significant intrinsic scatter. Other than a slow monotonic increase of γ_e with C_r , the slopes have little or weak dependence on C_r , M_* or n but systematically vary with R_{eff} . In other words, galaxy size appears to be a key indicator of global mass profiles. At a given mass, the smaller galaxy has a higher central density and thus a more steeply declining profile. We also find that slopes γ_p , γ_e and γ_{ih} are well correlated with the projected surface density $\Sigma_{\text{eff}} \equiv (M_*/2)/(2\pi R_{\text{eff}}^2)$ while γ_b is weakly correlated at best. The good correlation of γ_e with Σ_{eff} , which has already been noticed in the literature

(e.g. Auger et al. 2010; Dutton & Treu 2013), is consistent with the anti-correlation with R_{eff} . The lower right panel of Fig. 13 shows the distribution of the slopes against the host halo virial mass M_{200} . Slopes γ_p and γ_e are not well correlated with M_{200} . However, γ_{ih} declines systematically with M_{200} for $M_{200} \gtrsim 10^{12.5} M_{\odot}$ and γ_b has a good anti-correlation with M_{200} . These behaviours of γ_{ih} and γ_b imply that central galaxies contribute less to the total mass profile of more massive haloes. This can be attributed to the empirical property that the stellar-to-halo mass ratio M_*/M_{200} decreases with increasing M_{200} for $M_{200} \gtrsim 10^{12} M_{\odot}$ (e.g. More et al. 2011; Schulz, Mandelbaum & Padmanabhan 2010; Mandelbaum et al. 2006) while the size-to-virial radius ratio R_{eff}/r_{200} remains nearly constant (Kravtsov 2013). This can also be seen by Fig. 12 which shows that for more massive haloes the central stellar-to-DM density ratio is less boosted and consequently the NFW profile is retained over larger radial ranges.

5 SYSTEMATIC VARIATIONS

We consider possible systematic variations of our statistical results on mass profiles by varying the input ingredients including galaxy sample choice (with relevance to stellar mass profile and intrinsic galaxy shape), stellar IMF, stellar-to-halo mass relation, outer halo mass-concentration relation, velocity dispersion anisotropy profile, central sub-kiloparsec stellar mass profile, and DM profile functional form. We investigate how the statistical results are varied in response to a variation of each ingredient. We find that all varied results have similar curvature patterns in density slope profiles but have different values of characteristic density slopes. We also find that when inputs are varied, the resulting distribution of velocity dispersion profile slope η (equation 12) is also changed.

In Table 2 we list various input variations and the predicted values of $\langle \eta \rangle$ and $\langle \gamma_e \rangle$ (population mean slopes for the radial range $0.1R_{\text{eff}} < r < R_{\text{eff}}$). The important points are as follows:

(i) *The spherical symmetry assumption and galaxy sample choice:* We have a large number of galaxies selected by C_r , but empirical information for each galaxy is relatively limited compared with well-studied local ETGs (e.g. Cappellari et al. 2006; Thomas et al. 2007; Cappellari et al. 2013a). Because of the limit of our data we have assumed the spherical symmetry. We have then selected nearly spherical galaxies ($\epsilon < 0.15$) to minimize the error arising from the spherical symmetry assumption. In reality, even nearly spherical galaxies have in some cases non-negligible disk components in their light distributions. Because the presence of non-negligible disk components can invalidate the spherical symmetry assumption, we have further narrowed our selection by rejecting galaxies that have non-negligible disks. Our final sample of 2,054 nearly spherical, disk-less and $C_r > 2.86$ galaxies can be legitimately modelled relying on the spherical symmetry assumption.

However, there still remain a couple of issues. First, as we are modelling nearly spherical and disk-less galaxies only, our results may not hold for the general population of ETGs. For example, it is possible that intrinsic shapes of galaxies can increase the intrinsic scatter of the mass profile.

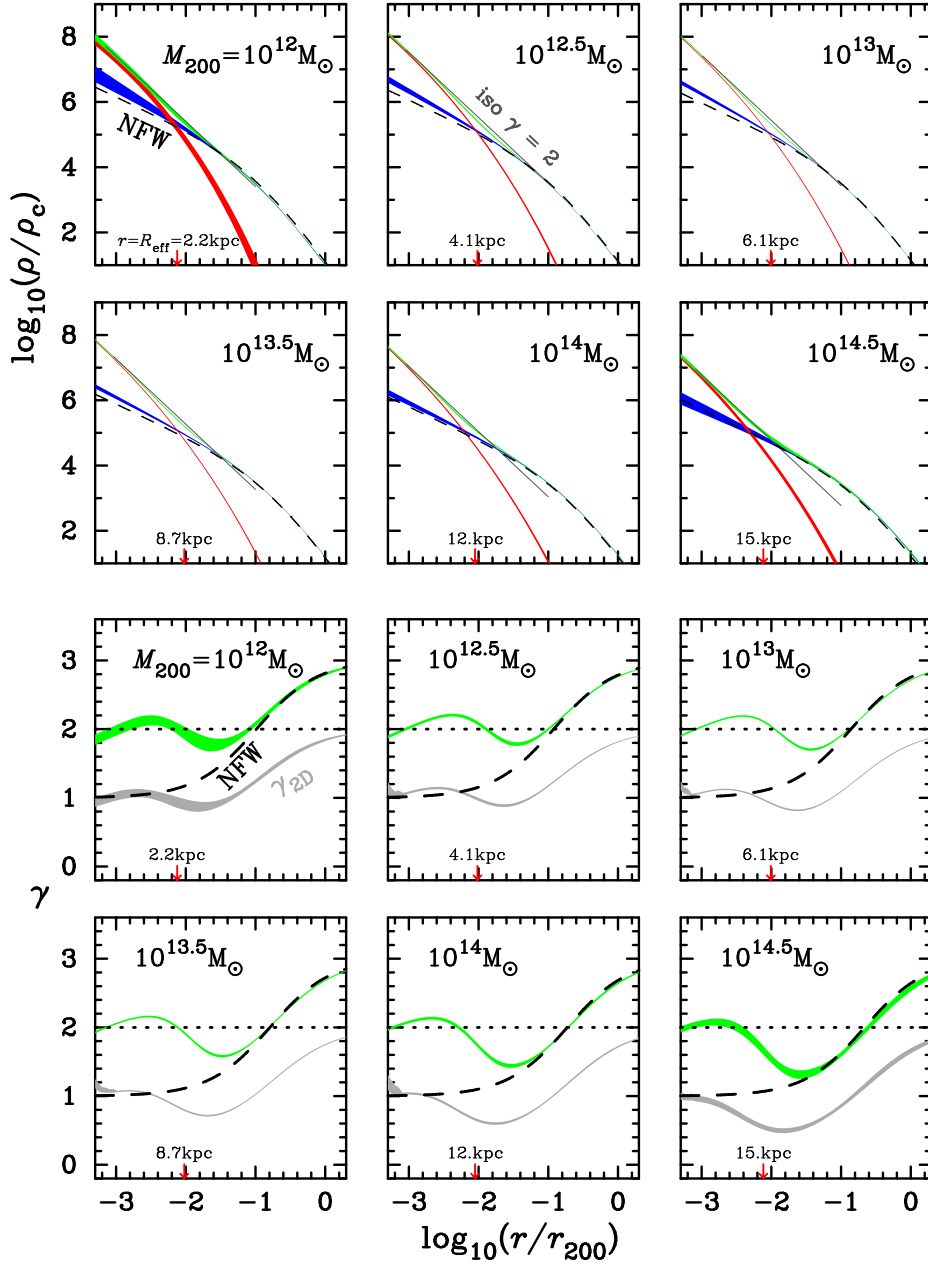


Figure 12. Density and slope profiles as in Fig. 11 for 6 sub-samples defined by halo virial mass M_{200} . Each sub-sample contains a number of nearly spherical galaxies within a range of ± 0.2 dex in M_{200} . In the upper half panels, red, blue and green regions represent respectively the 2σ uncertainties of the sample mean density profiles of stellar, DM and total mass in units of ρ_c , the critical density at $z = 0.12$. In the lower half panels, the green and gray regions represent respectively the slope profiles for the 3-dimensional and 2-dimensional projected total mass densities.

Second, all auxiliary empirical properties of ETGs (e.g. the IMF distribution, the $M_\star - M_{200}$ relation, the distributions of β and η) are for general populations of ETGs or red galaxies. If these properties are systematically different for spherical galaxies, then our results will be biased. However, we do not find any systematic difference between all ETGs and nearly spherical ETGs based on the literature data (see, e.g., Fig. 4 for the case of η).

As a way of estimating the systematic effects of non-spherical shapes we consider two samples of random ETGs.

One sample is drawn randomly from the $C_r > 2.86$ sample and the other sample from a sample with a relaxed criterion of $C_r > 2.6$. We also consider a $C_r > 2.6$ sample of nearly spherical and disk-less galaxies to see the pure effects of changing the C_r criterion. The results for the random $C_r > 2.86$ sample (fit # 3 in Table 2) have almost the same mean values of the slopes η and γ_e compared with the standard nearly spherical and disk-less sample (fit # 1) but have larger scatters in good agreement with the observed scatters for random ETGs. The $C_r > 2.6$ samples (fit # 4 & # 5)

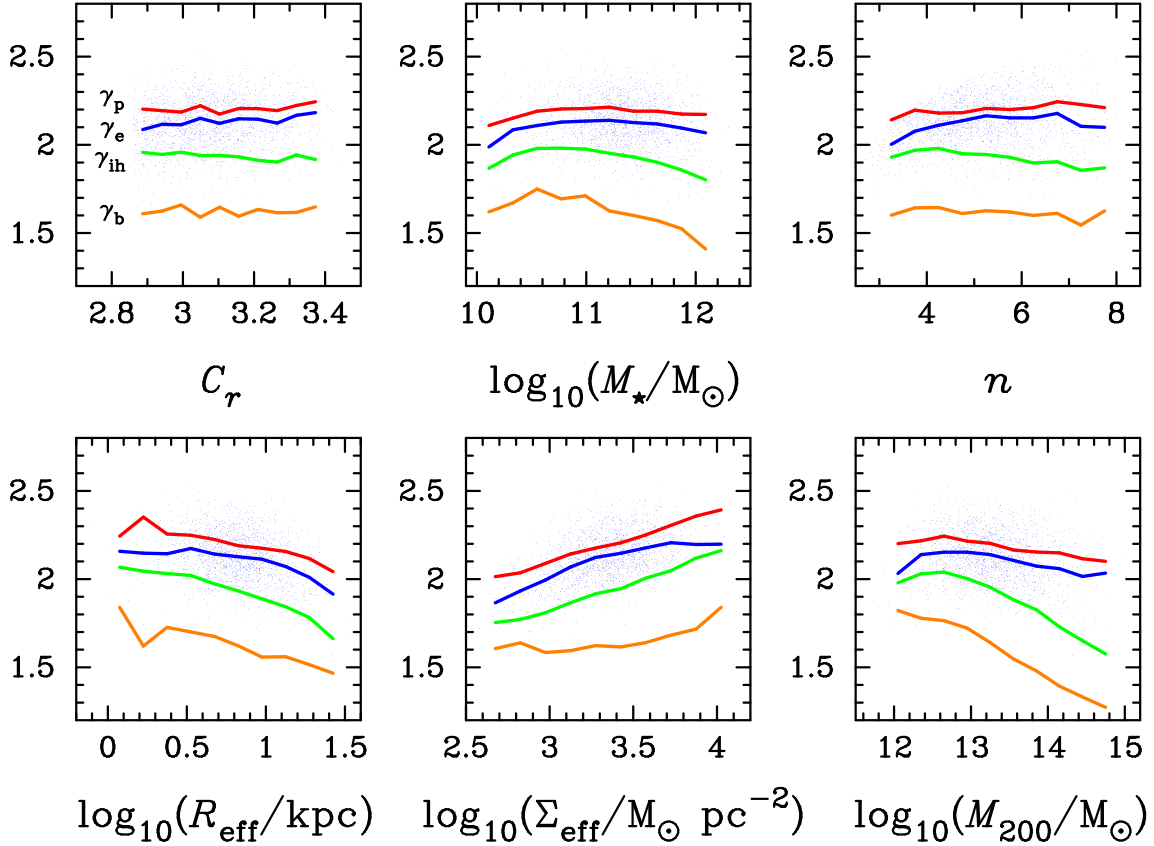


Figure 13. Four characteristic density slopes, γ_p , γ_e , γ_{ih} and γ_b shown in Fig. 10, against various parameters. Here C_r is the Petrosian light concentration in the r -band as described in section 2.2 and Σ_{eff} is the projected stellar mass density within R_{eff} .

have shallower mean slopes and larger scatters. In particular, the predicted values of the mean VP slope $\langle\eta\rangle$ are marginally discrepant with the empirical value $\langle\eta\rangle = -0.058 \pm 0.008$. Moreover, the random $C_r > 2.6$ sample (fit # 5) has larger scatter than observed.

(ii) *The assumption of parametric functional forms for DM distribution:* One of our underlying assumption is that the unknown DM distribution varies smoothly in radius and can be modelled by parametric functional forms motivated by N -body simulations combined with baryonic effects. Because it is an empirical fact that the outer halo where baryonic effects are negligible follows well the NFW functional form, we chose the gNFW model with a generalized central slope as our standard model. To see possible systematic errors of this assumption we also consider the Einasto model that is equally well motivated. We have checked that contracted haloes due to baryonic effects produced by state-of-the-art cosmological hydrodynamic simulations can be well approximated by the gNFW or the Einasto profile, as can be checked numerically using the Contra code (Gnedin et al. 2004, 2011). This means that if baryon-induced halo contraction effects are real, our models can mimic those effects. Also, note that our models can mimic effects of halo expansion as well if that occurs (for some galaxies). The result based on the the Einasto model (fit # 6) has somewhat shallower mean slopes compared with the standard result

(fit # 1) based on the gNFW model and interestingly larger scatter. Although the scatter of η is more consistent with the observed scatter than the standard result, the mean $\langle\eta\rangle$ is marginally shallower than the observed mean.

(iii) *Various empirical inputs:* We consider alternative choices of various empirical inputs, fit # 7 – # 14 in Table 2. The largest possible systematic differences are ≈ 0.006 - 0.008 in $\langle\eta\rangle$ and ≈ 0.03 - 0.05 in $\langle\gamma_e\rangle$ arising from the M_{\star}^{Ch} - M_{200} relation and the M_{200} - c_{NFW} relation. It is interesting to note that for the result using wildly varying VD anisotropies based on equation 5 has unchanging mean slopes but have almost twice larger scatter in η ($s_{\eta} = 0.055$ compared with $s_{\eta} = 0.028$) while keeping the scatter in γ_e nearly unchanged. This shows that anisotropy shapes can only affect the scatter of η but probably not the mean slopes.

(iv) *Correlations among empirical input parameters:* In our approach each galaxy with measured parameter values (σ_{ap} which is on average closest to σ_{e2} , R_{eff} , n , M_{\star}^{Ch}) is assigned various other parameter values [IMF variation with respect to the Chabrier IMF expressed in terms of $\delta_M = \log_{10}(M_{\star}/M_{\star}^{\text{Ch}})$, halo mass M_{200} , outer halo profile concentration expressed using the NFW profile c_{NFW} , anisotropy β (and velocity dispersion profile slope η for the chi-square approach)] using observed two-parameter relations including intrinsic scatter based on a wealth of empirical information. However, we ignored any possible mul-

Table 2. Various inputs and the resulting means of the luminosity-weighted LOSVD profile slope η and the mass density profile absolute slope γ_e in the optical region ($0.1R_{\text{eff}} < r < R_{\text{eff}}$). s_η and s_{γ_e} are the resulting scatters of the sample.

#	input	$\langle\eta\rangle$	s_η	$\langle\gamma_e\rangle$	s_{γ_e}
1	standard (Table 1)	-0.052	0.028	2.124	0.133
2	chi-square approach	-0.059	0.022	2.160	0.111
3	2,000 $C_r > 2.86$ random ETGs with single Sersic fits	-0.052	0.034	2.113	0.165
4	2,607 $C_r > 2.6$ EGs with $\varepsilon < 0.15$ & $\log_{10}(R_{\text{eff}}/R_{\text{bulge,eff}}) < 0.19$	-0.047	0.035	2.098	0.157
5	2,000 $C_r > 2.6$ random ETGs with single Sersic fits	-0.044	0.040	2.070	0.197
6	Einasto DM model	-0.046	0.034	2.094	0.163
7	IMF $\left\{ \begin{array}{l} \text{SPS} \\ \text{SPIDER} \end{array} \right.$	-0.056	0.028	2.142	0.131
8		-0.046	0.031	2.092	0.144
9	$M_\star^{\text{Ch}}-M_{200}$ $\left\{ \begin{array}{l} \text{weak lensing} \\ \text{abundance matching} \end{array} \right.$	-0.050	0.029	2.113	0.138
10		-0.058	0.028	2.152	0.126
11	$M_{200}-c_{\text{NFW}}$ $\left\{ \begin{array}{l} 30\%(\approx 2\sigma) \text{ higher} \\ 30\%(\approx 2\sigma) \text{ lower} \end{array} \right.$	-0.045	0.031	2.085	0.144
12		-0.060	0.027	2.170	0.126
13	radially varying $\beta(r)$	-0.051	0.055	2.131	0.139
14	$r_b/R_{\text{eff}} = 0.040 (M_\star^{\text{Ch}}/10^{11}M_\odot)^{-0.55}$	-0.058	0.032	2.123	0.139
15	R_{eff} -dependent η (Fig. 15) & β (Fig. 16)	-0.054	0.028	2.125	0.138

multiple correlations among input parameters. Here, we examine/discuss possible correlations and investigate how the mass profile results are affected.

First, when we assigned M_{200} to each galaxy, we used the observed $M_\star^{\text{Ch}}-M_{200}$ relation only. In doing so we ignored any possible correlations, in particular with σ_{e2} . To see possible effects of the ignored correlation with σ_{e2} we compare in Fig. 14 our posterior $M_{200}-\sigma_{e2}$ relation with the recent abundance matching output for which M_\star^{Ch} and σ_{e2}^1 were simultaneously assigned to $M_{\text{vir}} \sim 1.2 \times M_{200}$ taking into account correlations (Chae et al. 2012). Our posterior $\sigma_{e2}-M_{200}$ relation (data points and black line) deviates somewhat from the abundance matching relation (red line) in Chae et al. (2012), but the difference is certainly smaller than systematic differences due to the change of the $M_\star^{\text{Ch}}-M_{200}$ relation.

Second, when we assigned δ_M and c_{NFW} we used empirical relations respectively with σ_{e2} and M_{200} only. Similarly to the above case these assignments will have some systematic errors due to ignored correlations with other parameters. However, again the systematic errors arising from uncertainties of the $\sigma_{e2}-\delta_M$ and $M_{200}-c_{\text{NFW}}$ relations themselves are likely to be dominating.

Finally, when we assigned β (and η for the chi-square approach) we assumed no correlations at all. As shown in Fig. 4, η has no correlation with σ_{e2} for the ETGs that can match with our ETG samples. Fig. 15 shows η against R_{eff}

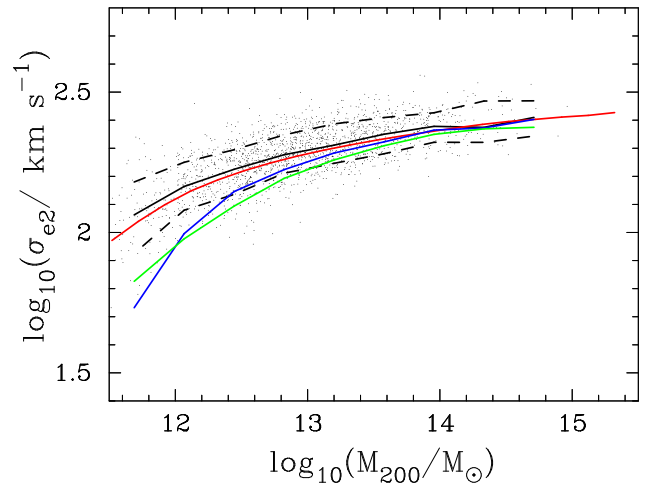


Figure 14. Data points and black curve show the posterior distribution of 2,054 SDSS nearly spherical galaxies for the modelling result with the abundance matching $M_\star^{\text{Ch}}-M_{200}$ relation (Table 2). (Dashed curves are 1σ scatters.) The red curve is the result of a bi-variate abundance matching of M_\star^{Ch} and σ_{e2} with M_{200} by Chae et al. (2012). The difference between the two is minor compared with the systematic differences with the results (blue and green curves) based on different $M_\star^{\text{Ch}}-M_{200}$ relations. Blue curve shows the result with standard $M_\star^{\text{Ch}}-M_{200}$ relation and green curve with weak lensing relation (Table 2).

¹ Chae et al. (2012) used σ_{e8} which has been converted to σ_{e2} here.

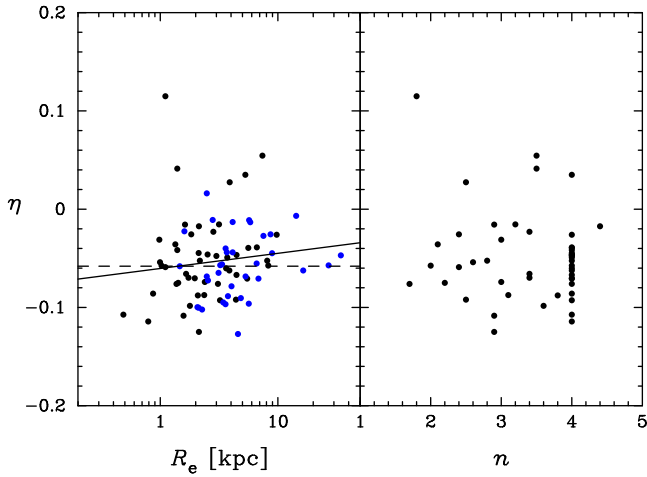


Figure 15. Distribution of η against R_{eff} and n for the galaxies shown in Fig. 4 except for $z \sim 0.25$ BCGs. Values of R_{eff} come from de Zeeuw et al. (2002) and Mehlert et al. (2000) respectively for black and blue data points. Values of n shown on the right-hand side come from Cappellari et al. (2007).

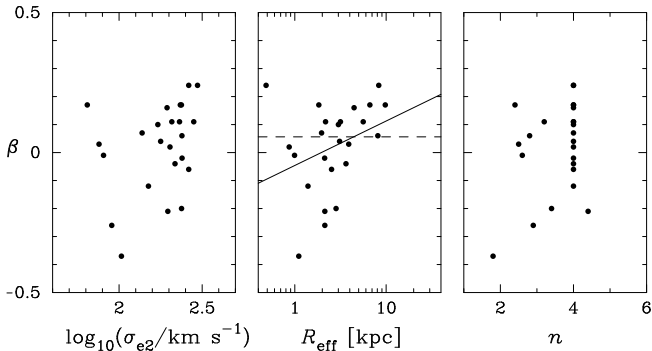


Figure 16. Distribution of constant anisotropy β for 24 nearby ETGs (a subsample of that shown in Fig. 4) modelled in Cappellari et al. (2007). There appears some trend with R_{eff} (solid line in the middle panel) based on this small sample. Values of R_{eff} and n come respectively from de Zeeuw et al. (2002) and Falcón-Barroso et al. (2011).

and n using available data in the literature. There is possibly a weak trend with R_{eff} as shown by a solid line but no correlation is found with n . Fig. 16 shows β against σ_{e2} , R_{eff} and n for 24 ETGs from Cappellari et al. (2007). There appears a trend with R_{eff} only but sample size is too small to be meaningful. Fig. 17 shows η against β and no correlation is found based on this small sample. To account for the effects of possible correlations of both β and η with R_{eff} we consider as an alternative choice the least-square fit relations shown in Fig. 15 and Fig. 16.

Fig. 19 shows the resulting distribution of $\langle \gamma_e \rangle$ against $\langle \eta \rangle$ for all 15 fits in Table 2. There is a good correlation between the two parameters. The tight correlation is remarkable considering that each result (or set of results)

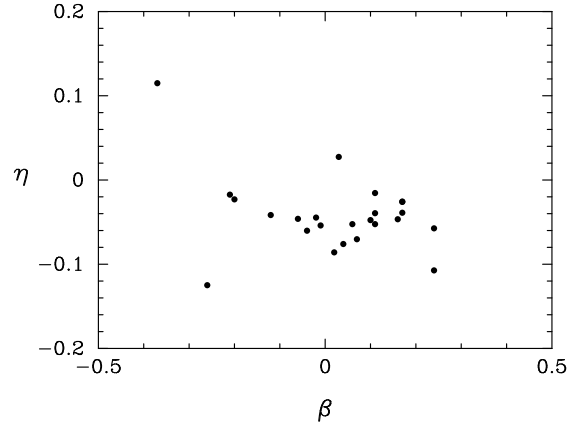


Figure 17. No correlation is found between β and η for 24 galaxies shown in Fig. 16.

was obtained by varying a different ingredient. Caring little about all the details of the inputs $\langle \gamma_e \rangle$ is essentially dictated by $\langle \eta \rangle$. This means that we can reliably estimate $\langle \gamma_e \rangle$ just by measuring $\langle \eta \rangle$ for an ETG sample without detailed dynamical modelling. The least-square fit relation is given by $\langle \gamma_e \rangle = a + b \langle \eta \rangle$ with $a = 1.865 \pm 0.008$ and $b = -4.93 \pm 0.15$. From our considered 15 different fits $2.07 \lesssim \langle \gamma_e \rangle \lesssim 2.17$ and $-0.060 \lesssim \langle \eta \rangle \lesssim -0.044$ along with $0.22 \lesssim s_\eta \lesssim 0.55$ and $0.11 \lesssim s_{\gamma_e} \lesssim 0.20$.

With our measured $\langle \eta \rangle = -0.058 \pm 0.008$ from section 2.6, we have $\langle \gamma_e \rangle = 2.15 \pm 0.04$. The value $\langle \eta \rangle = -0.066$ measured by Cappellari et al. (2006) corresponds to $\langle \gamma_e \rangle \approx 2.18$. Hence our results suggest a super-isothermal mean profile in the optical region with an intrinsic scatter of $0.1 \lesssim s_{\gamma_e} \lesssim 0.2$. Bolton et al. (2012) have recently carried out stellar dynamics plus strong lensing analyses of dozens of ETGs at $z \lesssim 0.6$. For 14 ETGs from Bolton et al. (2012) at a redshift range $0.05 < z < 0.15$ similar to our sample, we find $\langle \gamma_e \rangle = 2.242 \pm 0.034$ with $\sigma_{\gamma_e} = 0.121$. This result is even more steeper but consistent at a 2σ level with our results. Our results are somewhat ($\sim 2\sigma$) steeper than the mean profile of 16 Coma cluster ETGs, $\langle \gamma_e \rangle = 2.064 \pm 0.042$ with $\sigma_{\gamma_e} = 0.163$ (Thomas et al. 2007). However, if we consider only 9 normal ellipticals excluding lenticular and cD/D galaxies from the Coma cluster, the mean profile is $\langle \gamma_e \rangle = 2.134 \pm 0.049$ with $\sigma_{\gamma_e} = 0.137$ in closer agreement with our results. Our results are also somewhat steeper than, but consistent at a 2σ level with, the SLACS results (e.g. Auger et al. 2010; Barnabè et al. 2011): constant slope $\gamma = 2.074^{+0.043}_{-0.041}$ with $s_\gamma = 0.144^{+0.055}_{-0.014}$ (Barnabè et al. 2011). However, unlike the Bolton et al. (2012) result quoted above this result is for redshift range of $0.06 \lesssim z \lesssim 0.5$. As is discussed by Bolton et al. (2012) and in section 8 below, the inferred γ may depend on the redshift range, so that caution should be taken in comparing the SLACS results with our result.

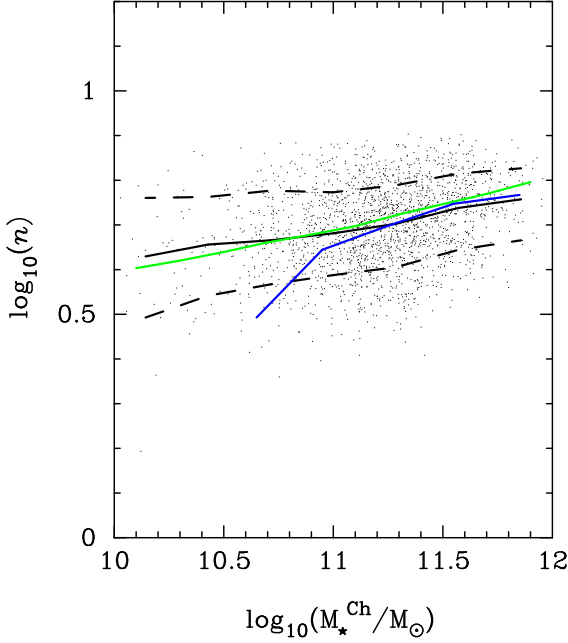


Figure 18. Distribution of Sérsic index n as a function of M_{\star}^{Ch} . Data points are 2,054 nearly spherical and disk-less galaxies of our standard sample that are well-described by a single Sérsic function with the prior $n \leq 8$. Black curve shows the median value and dashed curves show 1σ scatters. Green curve shows the median value for all 20,210 galaxies satisfying $C_r > 2.86$ with the prior $n \leq 8$, not all of which can be well described by a single Sérsic function. (This means that the distribution shown here for all ETGs is biased to some degree.) Blue curve is the median value for a published ETG sample based on a different selection by Guo et al. (2010).

6 COMPARISON WITH PREVIOUS DYNAMICAL ANALYSES RESULTS BASED ON SDSS APERTURE VELOCITY DISPERSIONS AND PHOTOMETRIC DATA

SDSS aperture velocity dispersions and photometric data have been widely used in the literature to infer dynamical masses and dark matter fractions in the optical region (e.g. Padmanabhan et al. 2004; Tortora et al. 2012) and to test halo contraction/expansion models and stellar IMFs (e.g. Schulz, Mandelbaum & Padmanabhan 2010; Dutton et al. 2011, 2013; Dutton & Treu 2013). It has been found that the SDSS data require non-universal IMFs and/or non-universal halo response to baryonic physics (Dutton et al. 2011, 2013; Dutton & Treu 2013). However, none of these studies have tried to predict mass profiles or considered velocity dispersion profiles, although Dutton & Treu (2013) have used the SLACS mass profile slope distribution ($\langle\gamma\rangle \approx 2.08$, $s_{\gamma} \approx 0.16$; Auger et al. 2010) to further study IMFs and halo response. Dutton & Treu (2013) argue that for massive ellipticals with mean $\log_{10}(\sigma_{e2}/\text{km s}^{-1}) = 2.40$ similar to the SLACS systems, uncontracted NFW haloes combined with the Salpeter IMF can reproduce the SLACS slope distribution. However, their argument depends on two assumptions that the SLACS slope distribution at higher redshifts can match low- z SDSS galaxies and the fiducial stellar mass

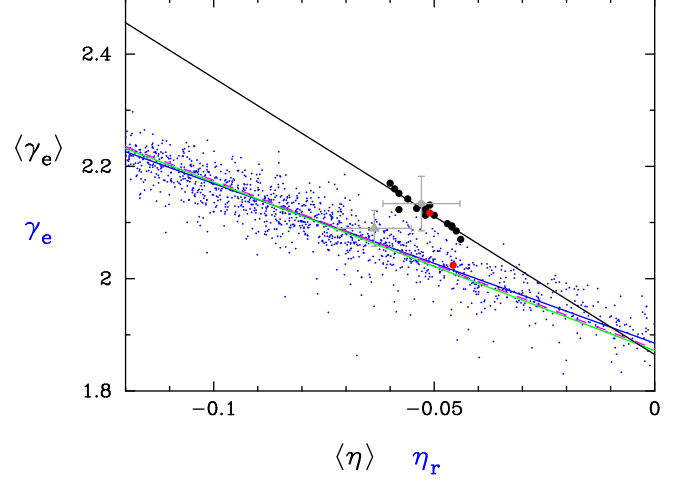


Figure 19. Predicted relation between mass and velocity dispersion slopes within R_{eff} for our fiducial model. Black points represent mean values for various modelling results obtained by varying model input ingredients. Two gray points with error bars represent the mean slopes for 9 normal ellipticals (filled circle) and 16 ETGs (filled triangle) of the Coma cluster using the models constructed by Thomas et al. (2007). Two red points represent the original and revised results based on a semi-empirical approach (Chae et al. 2012). Blue points represent individual slopes for the fiducial model. η and η_r respectively denote slopes for luminosity-weighted LOSVD (equation 11) and radial VD (equation 9). Black and blue lines are least-square fit results. The green line is the least-square fit result for the fixed slope of -3 . The dashed purple line is the relation predicted by the Bertschinger (1985) spherical infall model and produced for pure DM haloes by N -body simulations (Taylor & Navarro 2001).

based on the Chabrier IMF is correct (remember that M_{\star}^{Ch} itself is uncertain as mentioned in section 2.2). Nevertheless, the Dutton & Treu (2013) result differs by just $\sim 2\sigma$ from our best estimate and is within our systematic errors (cf. Table 2). In particular, it appears that if one fully considers realistic systematic errors halo contraction effects are inconclusive yet largely due to uncertainties in stellar masses involving IMFs (in preparation).

Recently a Jeans analysis of ETGs has been carried out by Chae et al. (2012) based on abundance matching between SDSS ETGs and the Bolshoi N -body simulation haloes (Klypin, Trujillo-Gomez & Primack 2011) and previously available statistical empirical properties of ETGs. The focus of that analysis was to compare the resulting DM profile (baryonic effects included) with the DM-only N -body simulation profile. A by-product was that mass profile slope values measured at $R_{\text{eff}}/2$ were on average close to isothermal. This is in contradiction with our steeper-than-isothermal profiles presented above. Specifically, for the case of using the same abundance matching $M_{\star}^{\text{Ch}}-M_{200}$ relation our new result ($\gamma_e \approx 2.15$ (fit # 10, Table 2) is steeper than ($\gamma_e \approx 2.02$ (the lower red point in Fig. 19) for a total of 3,000 ETGs (1,000 ETGs respectively of $M_{200} = 10^{12.5} M_{\odot}$, $10^{13} M_{\odot}$ and $10^{13.5} M_{\odot}$). Several factors can account for this difference.

First of all, as shown in Fig. 18 our newly measured val-

ues of Sérsic index n are higher than the previously adopted values (Guo et al. 2010) for $M_{\star}^{\text{Ch}} \lesssim 10^{11} M_{\odot}$. This is in part due to the difference in sample definitions. The Guo et al. (2010) sample includes low concentration spheroidal galaxies at low stellar masses while our sample includes only high concentration (i.e. $C_r > 2.86$) galaxies. When the semi-empirical approach is carried out with our new distribution of n for all ETGs (green curve) and the ATLAS^{3D} IMF distribution we have a higher $\langle \gamma_e \rangle \approx 2.12$ (the upper red point in Fig. 19).

The remaining difference of ≈ 0.03 can be attributed to other factors including differences in the posterior distribution of parameters (in particular R_{eff}) and their correlations owing to the different modelling procedure. In particular, in the semi-empirical approach the posterior distribution of η always had a mean shallower than -0.058 and was tried to approximately match $\langle \eta \rangle = -0.053$. Fig. 19 shows that the revised semi-empirical result falls right on the empirical $\langle \eta \rangle - \langle \gamma_e \rangle$ line while the original result deviates somewhat. In other words, whatever factors contributed to the difference in $\langle \gamma_e \rangle$ it can be explained by the difference in the posterior value of $\langle \eta \rangle$.

Despite the large difference in $\langle \gamma_e \rangle$ we find that total mass profiles from the semi-empirical analysis show similar curvature in the mean density slope profiles.

7 IMPLICATIONS FOR GALAXY FORMATION: UNIVERSAL PSEUDO-PHASE-SPACE DENSITY PROFILE?

The radial systematic pattern of each mass profile (Fig. 11, Fig. 12) and the systematic variation of the characteristic slopes (Fig. 13) as a function of some parameters, in particular the size and the projected effective surface density, implies that there is no natural attractor or strict conspiracy for total mass profiles of ETGs. The isothermal model is good only as a constant-slope approximation to the mean inner halo of the ETG population. ETGs are complex systems of luminous and dark matter and the interplay between them may create super-isothermal and sub-isothermal regions. When predictions of galaxy formation theories are compared with observed galaxies, the same radial ranges should be used and more importantly radially varying slopes may need to be considered.

The tight correlation between total mass and stellar VD slopes shown in Fig. 19 is reminiscent of the pseudo phase-space density profile for DM distribution produced by N -body simulations (Taylor & Navarro 2001). A universal power-law behaviour of the pseudo-phase-space density of DM (Taylor & Navarro 2001) given by $\rho_{\text{DM}}(r)/\sigma_{\text{DM}}^3(r) \propto r^{-\nu}$ ($\nu \approx 1.875$) implies $\gamma_{\text{DM}} = \nu - 3\eta_{\text{DM}}$ where $\sigma_{\text{DM}}(r)$ is the VD in the 3-dimensional physical space, $\gamma_{\text{DM}} = -d \ln \rho_{\text{DM}}(r)/d \ln r$, and $\eta_{\text{DM}} = d \ln \sigma_{\text{DM}}(r)/d \ln r$. A different slope of ≈ -4.93 in our relation $\langle \gamma_e \rangle \approx 1.86 - 4.93 \langle \eta \rangle$ can be attributed to the fact that $\langle \eta \rangle$ is for the LOSVD. Indeed, if we consider radial stellar VD $\sigma_r(r)$ (cf. equation 10) we recover a slope of ≈ -3 . Fig. 19 shows distributions of γ_e (total mass absolute slope within R_{eff}) and η_r ($\sigma_r(r)$ slope within R_{eff}) for our fiducial model. There is some intrinsic scatter but the least-square fit linear relation is $\gamma_e \approx 1.89 - 2.84\eta_r$

and $\gamma_e \approx 1.87 - 3\eta_r$ for the fixed slope of -3 which are very similar to the above relation for DM. This implies that there may exist a universal profile of pseudo phase-space density-like quantities in any collisionless components in dynamical equilibria (Chae 2013).

8 IMPLICATIONS FOR INTERPRETATION OF GRAVITATIONAL LENSING ANALYSES

Radially varying mass profiles of ETGs call for a careful interpretation of gravitational lensing, in particular strong lensing. Strong lensing depends on the projected 2-dimensional density slope γ_{2D} at the Einstein radius R_{Ein} . The redshift evolution of R_{Ein} in conjunction with the radial variation of the density slope (Fig. 12) can produce an apparent redshift evolution of a mass profile from an analysis of a strong lensing sample. Let us make a quantitative prediction based on a strong lens sample recently analysed by Bolton et al. (2012). The observed mean ratio $\langle R_{\text{Ein}}/R_{\text{eff}} \rangle$ evolves from ≈ 0.5 at $z = 0.1$ to ≈ 1 at $z = 0.55$ with a slope $d \log \langle R_{\text{Ein}}/R_{\text{eff}} \rangle / dz = 0.65 \pm 0.12$ while $\langle R_{\text{eff}} \rangle$ remains nearly unchanged (Bolton et al. 2012). According to our results for ETG mass profiles the mean density slope $\langle \gamma_{2D} \rangle$ varies as $d \langle \gamma_{2D} \rangle / d \log r = -0.45^{+0.14}_{-0.03}$ between $r = 0.5 R_{\text{eff}}$ and R_{eff} (Fig. 12), which gives $d \langle \gamma_{2D} \rangle / dz = -0.29^{+0.18}_{-0.12}$. Suppose we are using a constant-slope model for the lensing galaxy to fit the lensed image geometry and magnification ratios, then we would get $d \langle \gamma \rangle / dz = -0.29^{+0.18}_{-0.12}$ (note that for the constant slope profile $\gamma = \gamma_{2D} + 1$). The magnitude of this evolution is consistent (within $\sim 2\sigma$) with the reported evolution $d \langle \gamma \rangle / dz = -0.60 \pm 0.15$ from a combined analysis of strong lensing and stellar dynamics using a constant-slope model (Bolton et al. 2012). It is unclear whether this means the reported evolution is an artefact due to the radially varying slope or real because it was also based on stellar dynamics. However, our results indicate that it is possible that the reported evolution is due, at least in part, to the radially varying slope.

The density slopes at R_{eff} we derive are close to isothermal for massive ellipticals, though super-isothermal within R_{eff} , and are consistent with lens modelling results (Rusin, Kochanek & Keeton 2003) for intermediate redshift ($0.3 \lesssim z \lesssim 1$) strong lensing galaxies whose Einstein radii are on average close to R_{eff} .

9 CONCLUSIONS

Assembling statistically significant numbers of mass models of SDSS concentration-selected elliptical galaxies we find the following:

- Two-component mass models reproduce simultaneously the aperture velocity dispersion and the observed velocity dispersion profile slope distribution, but single-component mass models with constant or monotonically varying slope cannot successfully predict the observed velocity dispersion profile slope distribution without biasing the aperture velocity dispersion.
- For the region within R_{eff} there is a tight correlation between the mass density profile mean absolute slope $\langle \gamma_e \rangle$ and the velocity dispersion profile mean slope $\langle \eta \rangle$ as $\langle \gamma_e \rangle =$

$(1.865 \pm 0.008) + (-4.93 \pm 0.15)\langle\eta\rangle$ with little sensitivity to the details of the inputs and modelling procedures. From this relation one can estimate $\langle\gamma_e\rangle$ from a measurement of $\langle\eta\rangle$ without detailed dynamical modelling.

- The tight correlation between the density and VD profile slopes implies an approximately universal pseudo phase-space density power-law profile $Q(r) \equiv \rho(r)/\sigma_r^3(r) \propto r^\nu$ with $\nu \approx -1.87$, where $\rho(r)$ is the total mass profile and $\sigma_r(r)$ is the radial stellar VD.

- The radial variation of the total density slope we find in this study may result in an apparent redshift evolution of mass profile in strong lensing observations.

The findings presented in this paper can provide interesting constraints on galaxy formation models. In future studies it would be interesting to compare density and velocity dispersion profiles for galaxies forming in the concordance Λ CDM model and test whether they exhibit radial variation and correlation of slopes similar to those found in this study for observed galaxies.

We are grateful to Michele Cappellari, Charlie Conroy and Surhud More for providing their published and unpublished empirical results as tables. We thank them and Drew Newman for assistance in understanding their empirical results. We also thank Joshua Frieman for past collaboration and useful comments on an early draft. We gratefully acknowledge the anonymous referee's comments that helped us improve the manuscript significantly. MB acknowledges support from NASA grant ADP/NNX09AD02G. AVK acknowledges support by NSF and NASA via grants OCI-0904482 and NNX13AG81G and by the Kavli Institute for Cosmological Physics at the University of Chicago through grants NSF PHY-0551142 and PHY-1125897 and an endowment from the Kavli Foundation and its founder Fred Kavli.

REFERENCES

- Auger M. W., Treu T., Bolton A. S., Gavazzi R., Koopmans L. V. E., Marshall P. J., Moustakas L. A., Burles S., 2010, *ApJ*, 724, 511
- Barnabè M., Czoske O., Koopmans L. V. E., Treu T., Bolton A. S., 2011, *MNRAS*, 415, 2215
- Bell E. F., McIntosh D. H., Katz N., Weinberg M. D., 2003, *ApJS*, 149, 289
- Bernardi M., Meert A., Vikram V., Huertas-Company M., Mei S., Shankar F., Sheth R. K., *MNRAS*, submitted (arXiv:1211.6122)
- Bernardi M., Shankar F., Hyde J. B., Mei S., Marulli F., Sheth R. K., 2010, *MNRAS*, 404, 2087
- Bertschinger E., 1985, *ApJS*, 58, 39
- Binney J., Mamon G. A., 1982, *MNRAS*, 200, 361
- Binney J., Tremaine S., 2008, *Galactic Dynamics*, 2nd ed. (Princeton Univ. Press, Princeton, NJ).
- Blanton M. R., Roweis S., 2007, *AJ*, 133, 734
- Blumenthal G. R., Faber S. M., Flores R., Primack J. R., 1986, *ApJ*, 301, 27
- Bolton A. S., et al., 2012, *ApJ*, 757, 82
- Brimioulle F., Seitz S., Lerchster M., Bender R., Snigula J., *MNRAS*, in press (arXiv:1303.6287)
- Cappellari M., et al., 2006, *MNRAS*, 366, 1126
- Cappellari M., et al., 2007, *MNRAS*, 379, 418
- Cappellari M., et al., 2013, *MNRAS*, in press (arXiv:1208.3522)
- Cappellari M., et al., 2013, *MNRAS*, in press (arXiv:1208.3523)
- Chabrier G., 2003, *ApJL*, 586, 133
- Chae K.-H., 2011, *MNRAS*, 413, 887
- Chae K.-H., 2013, *ApJL*, submitted
- Chae K.-H., Kravtsov A. V., Frieman J. A., Bernardi M., 2012, *JCAP*, 11, 004
- Conroy C., van Dokkum P. G., 2012, *ApJ*, 760, 71
- Das P., Gerhard O., Churazov E., Zhuravleva I., 2010, *MNRAS*, 409, 1362
- de Zeeuw P. T., et al., 2002, *MNRAS*, 329, 513
- Duffy A. R., Schaye J., Kay S. T., Dalla Vecchia C., 2008, *MNRAS*, 390, 64
- Dutton A. A., et al., 2011, *MNRAS*, 416, 322
- Dutton A. A., Macciò A. V., Mendel J. T., Simard L., 2013, *MNRAS*, 432, 2496
- Dutton A. A., Treu T., arXiv:1303.4389
- Einasto J., Haud U., 1989, *A&A*, 223, 89
- Eisenstein D. J., et al., 2005, *ApJ*, 633, 560
- Faber S. M., et al., 1997, *AJ*, 114, 1771
- Falcón-Barroso J., et al., 2011, *MNRAS*, 417, 1787
- Frieman, J. A., Turner, M. S., Huterer, D., 2008, *ARA&A*, 46, 385
- Gallazzi A., Charlot S., Brinchmann J., White S. D. M., Tremonti C. A., 2005, *MNRAS*, 362, 41
- Gavazzi R., Treu T., Rhodes J. D., Koopmans L. V. E., Bolton A. S., Burles S., Massey R. J., and Moustakas L. A., 2007, *ApJ*, 667, 176
- Gerhard O., Kronawitter A., Saglia R. P., Bender R., 2001, *AJ*, 121, 1936
- Gnedin O. Y., Ceverino D., Gnedin N. Y., Klypin A. A., Kravtsov A. V., Levine R., Nagai D., Yepes G., 2011, *ApJ*, submitted (arXiv:1108.5736)
- Gnedin O. Y., Kravtsov A. V., Klypin A. A., Nagai D., 2004, *ApJ*, 616, 16
- Glass L., et al., 2011, *ApJ*, 726, 31
- Guo Y., et al., 2010, *MNRAS*, 404, 2087
- Hyde J. B., Bernardi M., Sheth R. K., Nichol R. C., 2008, *MNRAS*, 391, 1559
- Klypin A. A., Trujillo-Gomez S., Primack J., 2011, *ApJ*, 740, 102
- Komatsu E., et al., 2011, *ApJS*, 192, 18
- Kormendy J., Fisher D. B., Cornell M. E., Bender R., 2009, *ApJS*, 182, 216
- Krajinović D., et al., 2013, *MNRAS*, in press (arXiv:1210.8167)
- Kravtsov A. V., 2013, *ApJ*, 764L, 31
- Kroupa P., 2002, *Science*, 295, 82
- Loeb A., Peebles P. J. E., 2003, *ApJ*, 589, 29
- Lupton R., SDSS web site
<http://www.sdss.org/dr5/algorithms/sdssUBVRITransform.html>
- Lynden-Bell D., 1967, *MNRAS*, 136, 101
- Macciò A. V., Dutton A. A., van den Bosch F. C., Moore B., Potter D., Stadel J., 2007, *MNRAS*, 378, 55
- Mandelbaum R., Seljak U., Hirata C. M., 2008, *JCAP*, 08, 006
- Mandelbaum R., Seljak U., Kauffmann G., Hirata C. M., Brinkmann J., 2006, *MNRAS*, 368, 715
- Meert A., Vikram V., & Bernardi M., *MNRAS*, submitted (arXiv:1211.6123)

- Mehlert D., Saglia R. P., Bender R., Wegner G., 2000, *A&ASS*, 141, 449
- More S., van den Bosch F. C., Cacciato M., Skibba R., Mo H. J., Yang X., 2011, *MNRAS*, 410, 210
- Navarro J. F., et al., 2010, *MNRAS*, 402, 21
- Navarro J. F., Frenk C. S., White S. D. M., 1997, *ApJ*, 490, 493
- Newman A. B., Treu T., Ellis R. S., Sand D. J., Nipoti C., Richard J., Jullo E., 2013, *ApJ*, 765, 24
- Padmanabhan N. et al., 2004, *New A.*, 9, 329
- Percival W. J., et al., 2007, *MNRAS*, 381, 1053
- Prada F., Klypin A. A., Cuesta A. J., Betancort-Rijo J. E., Primack J., 2012, *MNRAS*, 423, 3018
- Press W. H., Schechter P., 1974, *ApJ*, 187, 425
- Prugniel P., Simien F., 1997, *A&A*, 321, 111
- Rest A., et al., 2001, *AJ*, 121, 2431
- Ruff A. J., et al., 2011, *ApJ*, 727, 96
- Rusin D., Kochanek C. S., Keeton C. R., 2003, *ApJ*, 595, 29
- Sánchez A. G., et al., 2012, *MNRAS*, 425, 415
- Schulz A. E., Mandelbaum R., Padmanabhan N., 2010, *MNRAS*, 408, 1463
- Sellwood J. A., McGaugh S. S., 2005, *ApJ*, 634, 70
- Sérsic J. L., 1968, *Atlas de Galaxias Australes* (Córdoba: Observatorio Astronómico)
- Taylor J. E., Navarro J. F., 2001, *ApJ*, 563, 483
- Thomas J., Saglia R. P., Bender R., Thomas D., Gebhardt K., Magorrian J., Corsini E. M., Wegner G., 2007, *MNRAS*, 382, 657
- Thomas J., Saglia R. P., Bender R., Thomas D., Gebhardt K., Magorrian J., Corsini E. M., Wegner G., Seitz S., 2011, *MNRAS*, 415, 545
- Tortora C., La Barbera F., Napolitano N. R., de Carvalho R. R., Romanowsky A. J., 2012, *MNRAS*, 425, 577
- Tortora C., Romanowsky A. J., Napolitano N. R., 2013, *ApJ*, 765, 8
- White S. D. M., Rees M. J., 1978, *MNRAS*, 183, 341
- York D. G., et al., 2000, *AJ*, 120, 1579

